



# Characteristic Curves of Polar Fluids: (I) The Two-Center Lennard–Jones Plus Dipole Fluid

Hans Renneis<sup>1</sup> · Simon Stephan<sup>1</sup>

Received: 16 March 2024 / Accepted: 31 March 2024  
© The Author(s) 2024

## Abstract

Brown's characteristic curves of polar fluids were studied using molecular simulation and molecular-based equation of state. The focus was on elucidating the influence of dipole interactions and the molecule elongation on the characteristic curves. This was studied using the symmetric two-center Lennard–Jones plus point dipole (2CLJD) model fluid class. This model class has two parameters (using Lennard–Jones reduced units), namely the elongation and the dipole moment. These parameters were varied in the range relevant for real substance models that are based on the 2CLJD model class. In total, 43 model fluids were studied. Interestingly, the elongation is found to have a stronger influence on the characteristic curves compared to the dipole moment. Most importantly, the characteristic curve results for the 2CLJD fluid are fully conform with Brown's postulates (which were originally derived for simple spherical dispersive fluids). The independent predictions from the computer experiments and the theory are found to be in reasonable agreement. From the molecular simulation results, an empirical correlation for the characteristic curves of the 2CLJD model as a function of the model parameters was developed and also applied for modeling real substances. Additionally, the intersection points of the Charles and Boyle curve with the vapor–liquid equilibrium binodal and spinodal, respectively, were studied.

**Keywords** Brown's characteristic curves · Equation of state · Molecular dynamics simulation · Polar interactions

---

✉ Simon Stephan  
simon.stephan@rptu.de

<sup>1</sup> Laboratory of Engineering Thermodynamics (LTD), RPTU Kaiserslautern, Erwin-Schrödinge-Straße 44, 67663 Kaiserslautern, Germany

## 1 Introduction

Permanent charge distributions in molecules induce polar interactions, which have an important effect on macroscopic properties. Charge distributions and the induced polar interactions are usually described in molecular models using multipole expansions [1, 2], i.e. point charges, point dipoles, point quadrupoles, point octupoles, etc. Especially point dipoles and point quadrupoles are frequently used since they are computationally significantly cheaper than the corresponding arrangement of point charges [3]. Moreover, it has been pointed out that higher-order multipoles yield a better physical description of electrostatic interactions than a corresponding arrangement of multiple point charges [4]. Polar interactions are relevant for many real substances [5–12]. Hence, modeling thermophysical properties of polar substances is important for many applications. For example, many refrigerant components and simple gases such as carbon monoxide and oxygen have important polar interactions [13–16]. Most importantly, higher order point multipoles, e.g. point dipoles and point quadrupoles, yield a strongly anisotropic interaction potential.

For the development and parametrization of fluid theories as well as for testing new simulation methods, model fluids play an important role [16–23]. Furthermore, model fluids enable systematic studies on the relation of specific molecular interactions and macroscopic properties [24–26], [27], [28–31]. Important model classes for small polar molecules are the two-center Lennard–Jones plus dipole (2CLJD) and the two-center Lennard–Jones plus quadrupole (2CLJQ) class. Models from these two classes comprise two Lennard–Jones interaction sites and a point dipole or point quadrupole. The two Lennard–Jones sites are at a given distance, named elongation  $L$ , which characterizes the shape of the molecule. The two Lennard–Jones interaction sites are identical regarding the dispersion energy  $\varepsilon$ , the size parameter  $\sigma$ , and the mass  $M$ . The point multipole interaction site is positioned at the center of mass of the model and has no mass itself. Accordingly, the 2CLJD or 2CLJQ model classes have four parameters: The dispersion energy  $\varepsilon$ , the size parameter  $\sigma$ , the elongation  $L$ , and the magnitude of the dipole  $\mu$  or quadrupole  $Q$ , respectively. Using the classical Lennard–Jones reduced units system [32], the number of parameters can be reduced to two [33, 34], i.e. the elongation and the multipole moment. These two polar fluid model classes can be used for modeling a large number of small polar molecules [8, 35]. These model classes have been used for systematically studying the influence of the elongation and the influence of the multipole moment magnitude on different thermophysical properties, e.g. phase equilibria [33, 34, 36–38], interfacial properties [39–44], transport properties [45–48], and virial coefficients [49, 50]. Thereby, high accurate global correlations for the vapor–liquid equilibrium and the surface tension are available today for the 2CLJD fluid class [34, 40]. Also, several perturbation theory models have been developed for polar model fluids [17, 51–55].

For many applications, thermophysical properties have to be modeled at extreme conditions regarding temperature and pressure, e.g. propulsion systems [56], geology [57, 58], and tribology [59–61]. Models from molecular

thermodynamics can be often used for predicting thermophysical properties at conditions that were not considered for the model development. Yet, their thermodynamic consistency can not be taken for granted. For the assessment of the thermodynamic consistency of models at extreme conditions, *Brown's* characteristic curves can be used [62]. In this sequel of two papers, we study *Brown's* characteristic curves for the 2CLJD and 2CLJQ fluid. In this first part, we study the 2CLJD model class; the second part focuses on the 2CLJQ model class. In this work, we study *Brown's* characteristic curves of the 2CLJD model class.

The characteristic curves were postulated by *Brown* [62] and represent the loci of state points at which a specific thermodynamic property of the fluid matches that of an ideal gas (details below). Based on rational thermodynamic arguments, *Brown* postulated that these curves have certain features for simple dispersive fluids. *Brown* introduced the characteristic curves also as a method for the assessment of thermodynamic models. The testing of these characteristic curves has been incorporated into the guidelines established by the International Union of Pure and Applied Chemistry (IUPAC) for publishing equations of state (EOS) [63] and is widely used today in that context [64–75]. Despite the fact that *Brown* derived the conditions for the characteristic curves for simple fluids, i.e. spherical particles with simple repulsive and dispersive interactions, the test procedure is also applied to complex molecules that comprise an elongation, polar interactions or association [65, 66, 69, 70, 75]. Interestingly, the applicability and transferability of *Brown's* arguments to molecules comprising complex interactions such as polar interactions induced by point multipoles has not been studied yet. In this work, we study *Brown's* characteristic curves for the 2CLJD model class to assess the validity of his arguments for polar fluids.

There is practically no experimental data for *Brown's* characteristic curves available today. Yet, *Brown's* characteristic curves can be obtained from molecular simulations [76, 77]. While some data are available for the Charles curve (a.k.a. Joule-Thomson inversion curve) [78–87], information for the other characteristic curves is still scarce. Systematic studies for *Brown's* characteristic curves have been carried out for simple fluids such as the Lennard–Jones and the Mie model fluids [73, 77].

In this work, we use molecular simulation and a molecular-based EOS model for determining *Brown's* characteristic curves for a large range of 2CLJD models. In total, 43 2CLJD fluids were studied for elucidating the influence of the elongation  $L$  and the dipole moment  $\mu$  on the characteristic curves. For the molecular simulations, the method proposed in an earlier work of our group [77] was used. For the molecular-based EOS, the 2CLJ model proposed by *Lisal et al.* [88] was used in combination with the dipole term proposed by *Gross and Vrabec* [17]. Additionally, accurate empirical correlations of the molecular simulation characteristic curve results were developed as global functions of the model parameters. Moreover, the empirical model is exemplarily applied to describe real substances. As an additional focus of this paper, the intersection points of the Boyle and Charles curve with the VLE binodal and spinodal were studied.

This work is outlined as follows: First, a brief introduction to *Brown's* characteristic curves and their conditions for a thermodynamically consistent model are summarized; then, the 2CLJD molecular model class and the simulation method and the



limit  $\rho \rightarrow 0$ . The Zeno curve intersects the three first-order curves in a single point. For many substances, the intersection point of the Zeno and Amagat curve lies in the solid region. The intersection point of the Zeno and Boyle curve is the common zero-density limit. The three first-order curves, on the other hand, must not intersect each other, but enclose each other in a  $p - T$  projection. The Charles and Boyle curve intersect the vapor-liquid equilibrium (VLE) binodal and spinodal, respectively, cf. Figure 1. The zero-density limit of the characteristic curves are related to specific conditions of the virial coefficients. The corresponding characteristic zero-density temperature values are denoted as  $T_{\text{char}}$ . The common zero-density limit characteristic point of the Boyle and Zeno curve is located at  $T_{\text{char,Boyle}} = T_{\text{char,Zeno}}$ , often referred to as the Boyle temperature, where the second virial coefficient is zero

$$B(T_{\text{char,Boyle}}) = 0. \quad (1)$$

For the Amagat curve, the zero-density limit is located at the temperature  $T_{\text{char,Amagat}}$ , where the second virial coefficient  $B$  reaches its maximum value, i.e.

$$T_{\text{char,Amagat}} = T(B_{\text{max}}). \quad (2)$$

The zero-density characteristic point of the Charles curve is located at the temperature  $T_{\text{char,Charles}}$ , where the condition

$$\partial B / \partial T = B(T_{\text{char,Charles}}) / T_{\text{char,Charles}} \quad (3)$$

holds.

State points on the characteristic curves exhibit specific values regarding the compressibility factor  $Z$  and its derivatives with respect to the temperature  $T$ , pressure  $p$ , and density  $\rho$ . Along the Zeno curve, state points satisfy the condition

$$Z = \frac{p}{\rho TR} = 1. \quad (4)$$

For the first-order characteristic curves, the derivative of the compressibility factor  $Z$  with respect to temperature, pressure, and specific volume are zero, i.e.

$$\left( \frac{\partial Z}{\partial T} \right)_v = 0, \quad (5)$$

for the Amagat curve,

$$\left( \frac{\partial Z}{\partial p} \right)_T = 0, \quad (6)$$

for the Boyle curve, and

$$\left( \frac{\partial Z}{\partial v} \right)_p = 0, \quad (7)$$

for the Charles curve. The four criteria (4)–(7) can be transferred to different thermodynamic properties using classical thermodynamic relations, cf. Refs. [72, 74–76] for details.

### 3 Investigated 2CLJD Fluids

The potential model of the 2CLJD fluid is defined as

$$u_{2CLJD}(r_{ij}, \omega_i, \omega_j, L, \mu^2) = u_{2CLJ}(r_{ij}, \omega_i, \omega_j, L) + u_D(r_{ij}, \omega_i, \omega_j, \mu^2), \quad (8)$$

with  $u_{2CLJ}$  being the potential of the two-center Lennard–Jones model and  $u_D$  being the point dipole potential. The interaction potential of the 2CLJ model can be written as

$$u_{2CLJ}(r_{ij}, \omega_i, \omega_j, L) = \sum_{a=1}^2 \sum_{b=1}^2 4\epsilon \left[ \left( \frac{\sigma}{r_{ab}} \right)^{12} - \left( \frac{\sigma}{r_{ab}} \right)^6 \right], \quad (9)$$

where  $\sigma$  and  $\epsilon$  are the size and the energy parameter of the Lennard–Jones potential, respectively, and  $r$  is the distance between interaction sites of two molecules  $i$  and  $j$ . The distance between the four distinct site-site possibilities is represented by  $r_{ab}$ :  $a$  represents the two sites of molecule  $i$ ,  $b$  the two sites of molecule  $j$ . The point dipole interactions can be written as

$$u_D(r_{ij}, \omega_i, \omega_j, \mu^2) = \frac{1}{4\pi\epsilon_0} \frac{\mu^2}{|r_{ij}|^3} (\cos \gamma_{ij} - 3 \cos \theta_i \cos \theta_j), \quad (10)$$

where the orientations of the two molecules  $i$  and  $j$  are represented by  $\omega_i$  and  $\omega_j$ . The angles between the dipole moments  $\mu_i$  and  $\mu_j$  and their corresponding distance vector  $r_{ij}$  are represented by  $\theta_i$  and  $\theta_j$ .

In this work, only symmetric 2CLJD fluids were studied, i.e. the two Lennard–Jones sites have identical  $\epsilon$ ,  $\sigma$ , and mass  $M$ . Moreover, the direction of the point dipole was in all cases along the axis of the two Lennard–Jones sites. Hence, the 2CLJD model has four parameters, namely the size parameter  $\sigma$ , the energy parameter  $\epsilon$ , the site-site distance of the two Lennard–Jones sites, i.e. the elongation  $L$ , and the dipole moment  $\mu$ . By using the Lennard–Jones units system, all results are represented with respect to the Lennard–Jones parameters  $\epsilon$  and  $\sigma$ . Therefore, the 2CLJD model system can be reduced to a two-parameter model, namely, the dimensionless elongation  $L/\sigma$  and the dimensionless (squared) dipole moment  $\mu^2/(4\pi\epsilon_0\epsilon\sigma^3)$ . Moreover, the convention  $4\pi\epsilon_0 = 1$  [40] is adopted for simplification of the notation.

In total, 43 2CLJD model fluids were studied, covering a wide range of  $L$  and  $\mu$ . Figure 2 shows the parameter space covered in this work in comparison to real substance model parameters for various substances available in the literature [5–8, 14–16]. The reduced elongation was studied in the range  $L/\sigma = 0, 0.2, 0.4, 0.505, 0.6, 0.8, 1$ . The reduced squared dipole moment was studied in the range  $\mu^2/\epsilon\sigma^3 = 0, 3, 6, 9, 12, 16, 20$ .

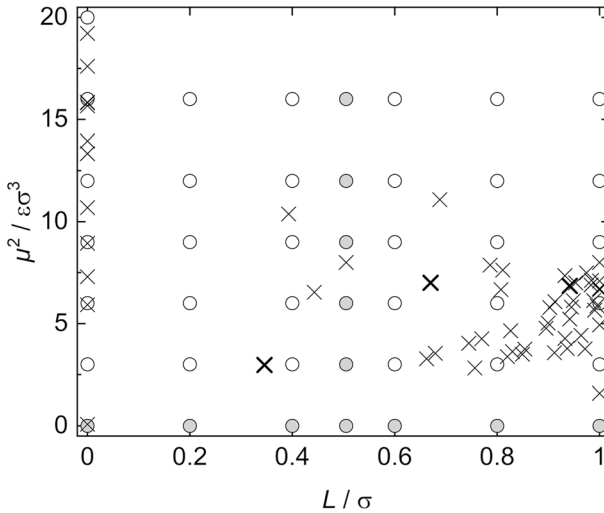


**Fig. 2** Parameters for 2CLJD model fluids: The model fluids investigated in this work are represented by circles. Filled circles indicate fluids focused on in the results section of this work. Crosses indicate model parameters of real substance models from the literature [5–7, 14–16]. Thick crosses indicate real substance models discussed below

## 4 Methods

### 4.1 Molecular Simulations

In this work, *Brown's* characteristic curves were determined using the simulation approach proposed by *Urschel and Stephan* [77]. This method consists of three steps: (i) calculating the zero-density limit  $\rho \rightarrow 0$  characteristic temperatures and determining initial guess values from a molecular-based EOS; (ii) performing MD simulations in the vicinity of the initial guess values for determining the characteristic curve state points, and (iii) assessing the thermodynamic consistency of the results. All molecular simulations in this work were carried out with the simulation engine *ms2* [89, 90].

The initial guess characteristic curves (i) were computed using a molecular-based EOS (details given below) corrected with the virial coefficient from the force field [77]. The second virial coefficient of a given molecular force field model was sampled using Monte Carlo (MC) simulations and the results were used for fine-tuning the initial guess characteristic curves obtained from the EOS – as proposed in Ref. [77]. The second virial coefficient  $B(T)$  was sampled using MC simulations from the intermolecular potential  $u_{2\text{CLJD}}$ , cf. Equation 8 with

$$B(T) = -2\pi \int_0^\infty \left\langle \exp\left(-\frac{u_{2\text{CLJD}}(r_{ij}, \omega_i, \omega_j, L, \mu^2)}{k_B T}\right) - 1 \right\rangle_{\omega_i, \omega_j} r_{ij}^2 dr_{ij}. \quad (11)$$

where  $T$  is the temperature. Equation 11 was evaluated for a wide temperature range. For each temperature, Eq. 11 was evaluated at 200 distances  $r_{ij}$  between the center of mass of two molecules in the range  $r_{ij,\min} = 0.2$  and  $r_{ij,\max} = 20$ . For each distance, 1,000 random orientations were evaluated. For each temperature, 10 replica simulations were carried out using different random seeds for the MC simulations. From the results, the average was computed. The results for  $B(T)$  were fitted to the empirical correlation proposed by Xu *et al.* [91] and evaluated at the conditions for the zero-density characteristic points, cf. Equations 1–3.

For determining characteristic curve state points, in step (ii), sets of simulations at given temperatures were carried out in the vicinity of the initial guess values. For determining characteristic curve state points, different simulation routes (ensembles, thermodynamic definitions etc.) are in general feasible that were systematically compared in Ref. [77]. We followed the suggestion from Ref. [77] and used NVT simulation sets for determining Zeno, Boyle, and Charles curve state points and NpT simulations for determining Amagat curve state points. The simulation sets were evaluated based on the following criteria:  $Z = 1$  for the Zeno curve,  $(\partial U/\partial V)_T = 0$  for the Amagat curve,  $(\partial Z/\partial V)_T = 0$  for the Boyle curve, and  $(\partial H/\partial p)_T = 0$  for the Charles curve. For each 2CLJD model fluid, at least nine characteristic curve state points were determined for a given characteristic curve. The statistical uncertainties of a characteristic curve state point were determined using an error propagation technique [77].

An additional NVT simulation was performed in step (iii) for each characteristic curve state point obtained in step (ii) to calculate additional thermodynamic properties and carry out a consistency test. For these simulations, the *Lustig* formalism [90, 92, 93] was applied in the simulations, which yields the derivatives of the reduced Helmholtz energy per particle  $\tilde{a}_{kl}$  with  $\tilde{a} = A/(Nk_B T)$ . For the Helmholtz energy derivatives, a short hand notation is used:

$$\tilde{a}_{kl} = (1/T)^k \rho^l \frac{\partial^{k+l} \tilde{a}}{\partial (1/T)^k \partial \rho^l}. \quad (12)$$

From the sampled Helmholtz energy derivative values, the thermodynamic consistency of the characteristic curve state points can be assessed [77]. The Zeno curve is evaluated from the condition  $\tilde{a}_{01} = 0$ , the Amagat curve from  $\tilde{a}_{11} = 0$ , the Boyle curve from  $\tilde{a}_{01} + \tilde{a}_{02} = 0$ , and the Charles curve from  $\tilde{a}_{01} + \tilde{a}_{02} + \tilde{a}_{11} = 0$ .

The MD simulations were carried out with 2,000 particles in a cubic box using periodic boundary conditions. The equilibration was performed with 100,000 time steps for NVT and an additional 100,000 time steps for NpT equilibration. The production run consisted of 750,000 time steps. The cut-off radius was  $5\sigma$ . For the cut-off, the *center of mass* method was used. The time step was set to  $\Delta\tau = 0.0005\sigma\sqrt{M}/\varepsilon$ . Classical long-range corrections were employed. For the thermostat, classical velocity scaling was used. For prescribing the pressure, Andersen's barostat was applied. The barostat piston mass was specified by the heuristic approach proposed in Ref. [77].



## 4.2 Molecular-Based Equation of State

For modeling thermodynamic properties of the 2CLJD fluids, a molecular-based EOS model built from the Helmholtz energy terms proposed by *Lísal et al.* [88] and *Gross and Vrabec* [17] was used. In the EOS model, the configurational Helmholtz energy per particle  $a_{\text{config}} = A_{\text{config}}/N$  is written as

$$\frac{a_{\text{config}}^{2\text{CLJD}}}{k_{\text{B}}T} = \tilde{a}_{\text{config}}^{2\text{CLJD}}(T, \rho, L, \mu) = \tilde{a}_{2\text{CLJ}}(T, \rho, L) + \tilde{a}_{\text{D}}(T, \rho, \mu), \quad (13)$$

where  $\tilde{a}_{2\text{CLJ}}$  represents the Helmholtz energy contribution of the 2CLJ reference fluid and  $\tilde{a}_{\text{D}}$  the contribution for dipole interactions. For  $\tilde{a}_{2\text{CLJ}}$ , the model proposed by *Lísal et al.* [88] was used. For  $\tilde{a}_{\text{D}}$ , the model proposed by *Gross and Vrabec* [17] was used. The 2CLJ term of *Lísal et al.* [88] consists of a hard sphere term and a semi-empirical perturbation dispersion term. For the hard sphere term, the model from *Boublík and Nezbeda* [94] is used. The parameters of the 2CLJ term were determined from a fit to both homogeneous state property data at moderate conditions and VLE data [88]. The dipole term of *Gross and Vrabec* [17] is formulated as a third-order perturbation theory Padé approximation. The parameters of the dipole term were fitted to VLE data for 2CLJD fluids [17]. The EOS model defined by Eq. 13 was used in this work for computing the characteristic curves as well as the VLE binodal and spinodal of all studied fluids.

## 4.3 Empirical Correlation for Characteristic curves

Based on the computer experiment results for the characteristic curves of the 2CLJD fluid class, a global empirical correlation was developed. Empirical correlations for the Zeno, Amagat, Boyle, and Charles curve were developed individually. The empirical correlation describes the pressure of the characteristic curve as a function of the temperature using reduced variables with respect to the critical point, i.e.  $p^* = p/p_c$  and  $T^* = T/T_c$ . The empirical model is written as

$$\begin{aligned} p_i^* = & a (T^* - T_{\text{char},i}^*) \\ & + b_i (T^* - T_{\text{char},i}^*)^2 \\ & + c_i (T^* - T_{\text{char},i}^*)^3 \\ & + d_i \tanh(0.1(T^* - T_{\text{char},i}^*)) \\ & + e_i (\exp(0.1(T^* - T_{\text{char},i}^*)) - 1), \end{aligned} \quad (14)$$

where  $a, b, c, d, e$  indicate fitting parameters and  $T_{\text{char},i}^*$  is the reduced zero-density limit characteristic temperature for each curve  $i = \text{Zeno, Amagat, Boyle, and Charles}$ . All properties are reduced with respect to the critical point data, which is obtained from the correlation of *Stoll et al.* [34] that describes the critical pressure and critical temperature as global functions of the model class parameters, i.e.  $T_c = T_c(L, \mu)$  and  $p_c = p_c(L, \mu)$ .

The empirical ansatz function used for describing the characteristic curves, cf. Equation 14, comprises the zero-density limit  $T_{\text{char},i}^* = T_{\text{char},i}/T_c$ . Also the zero-density limit  $T_{\text{char},i}$  was modeled here as a global function of the model class parameters, i.e.  $T_{\text{char},i} = T_{\text{char},i}(L, \mu)$ . We use the empirical ansatz function proposed by Vega *et al.* [50]:

$$\begin{aligned} T_{\text{char},i}(L, \mu) = & (d_1 + d_2L + d_3L^2 + d_4L^3 + d_5L^4) \\ & + \mu((f_1 + f_2L + f_3L^2) \\ & + (f_4 + f_5L + f_6L^2)\mu \\ & + (f_7 + f_8L + f_9L^2)\mu^2 \\ & + (f_{10} + f_{11}L + f_{12}L^2)\mu^3), \end{aligned} \quad (15)$$

where  $d_i$  and  $f_i$  indicate fitting parameters. The obtained parameters of the empirical model are given in Table 2 and 3.

Equations 14 and 15 were used for modeling the characteristic curves in the pressure-temperature projection, i.e.  $p^* = p^*(T^*)$ . In the Supplementary Material, additional empirical correlations are presented for the density-temperature projection, i.e. for describing  $\rho^* = \rho^*(T^*)$  for the Amagat, Charles, and Boyle curve. For the Zeno curve, the density can be obtained directly by evaluating the thermodynamic condition  $Z = 1$  in combination with the pressure model  $p^* = p^*(T^*)$ . An implementation of the empirical correlation is given in the electronic Supplementary Material.

#### 4.4 Intersection of Boyle and Charles Curve with the Vapor–Liquid Equilibrium

The zero-density limit constitutes the endpoint of the characteristic curves at high temperatures and can be obtained straightforwardly from the virial route. The Amagat and Zeno curve have their starting point in the solid phase region. The Boyle and Charles curve, on the other hand, start on the vapor-liquid binodal and spinodal, respectively (cf. Figure 1).

From the characteristic curve results and the results for the vapor-liquid equilibrium of the 2CLJD fluid, the intersection point of the Boyle curve with the spinodal as well as the intersection point of the Charles curve with the binodal were determined. As an example, this evaluation was applied for the 2CLJD fluid with  $L/\sigma = 0.505$  and  $\mu^2/\varepsilon\sigma^3 = 6$ . For both the Boyle and the Charles curve of that 2CLJD fluid, five characteristic curve state points were determined with the molecular simulation method (see above) in the range  $0.6T_c$  to  $0.9T_c$ , where  $T_c$  is the critical temperature. The critical point was determined from the empirical correlation of Stoll *et al.* [34]. For the Charles curve, the intersection point of the empirical correlation (describing the computer experiment data) and the binodal was computed, where the binodal was taken from the empirical correlation proposed by Stoll *et al.* [34]. For the Boyle curve, the intersection point of the empirical correlation and the spinodal was computed, where the spinodal was taken from the EOS model described by Eq. 13.

Performing MD simulations near the critical point and in the metastable region is challenging, e.g. phase separation is encountered regularly. This was monitored by checking the structure in the simulations and only simulations comprising homogeneous phases were used for the evaluation of the characteristic curve state points in step (ii).

## 5 Results

The results section is outlined as follows: First, the results for the zero-density limit characteristic points are presented and discussed. Then, the results for the characteristic curves of a representative part of the 2CLJD fluids (cf. grey filled symbols in Fig. 2) as well as the application to real substances are presented and discussed. The numerical data for the molecular simulation results for all studied 2CLJD fluids are reported in the Supplementary Material.

### 5.1 Zero-Density Limit Characteristic Points

Figure 3 shows the results for zero-density limit characteristic points of the Zeno, Amagat, Charles, and Boyle curve obtained from the virial route for the studied 2CLJD fluids. For the vast majority of points, the error bars are within the symbol size. Data for the Boyle temperature for different 2CLJD fluids have also been reported by Vega *et al.* [50]. Our results are in good agreement with their results.

An interesting observation arises when considering a given elongation for a given characteristic curve: The zero-density limit characteristic points increase with the strength of the dipole moment  $\mu$ . For the Boyle temperature, this effect was reported previously by Vega *et al.* [50]. As the strength of the dipole moment increases, attractive forces between molecules become stronger, eventually reaching

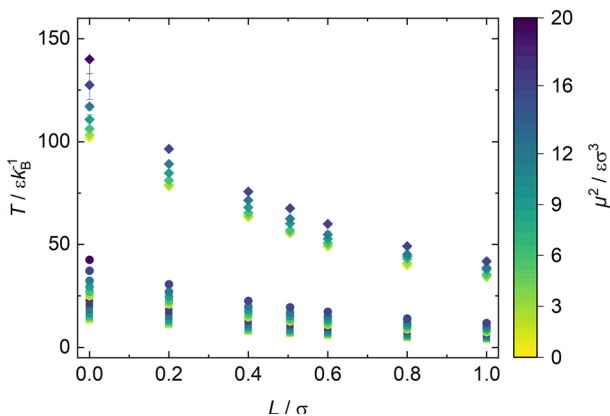


**Fig. 3** Temperature of the zero-density limit characteristic points of the 2CLJD fluids. Diamonds indicate the zero-density limit characteristic point for the Amagat curve, bullets for the Charles curve, and squares for the Boyle curve. Error bars are only given if they exceed the symbol size

a point, where attractive and repulsive forces cancel out at the Boyle temperature. On the other hand, for a constant dipole moment, an increasing elongation  $L$  leads to a noticeable decrease of the temperature of the zero-density characteristic point, resulting in a shift towards lower temperatures.

Overall, the elongation has a stronger influence than the dipole moment – in the studied ranges. For the studied elongation range, the temperature of the zero-density limit characteristic points varies in the range  $T_{\text{char},i}^* = 2.. 3 \epsilon k_B^{-1}$ ; for the studied dipole moment range, the temperature of the zero-density limit characteristic points lies in the range  $T_{\text{char},i}^* = 1.2.. 1.5 \epsilon k_B^{-1}$ .

## 5.2 Brown's Characteristic Curves

Figure 4 shows the characteristic curve results for a selection of 2CLJD fluids in the classical double-logarithmic  $p - T$  projection. Results from both computer experiment and the EOS are shown. The results for the 2CLJD fluids are fully conform with *Brown's* postulates for the topology of the characteristic curves (originally derived for simple fluids). The same holds for all other studied 2CLJD fluids, see Supplementary Material. The 2CLJD characteristic curves exhibit infinite slope in the zero-density limit, no intersection for the Amagat, Charles, and Boyle curve, a single intersection of the Zeno curve with the Amagat, Charles, and Boyle curve etc. Hence, the elongation and the dipole moment of the 2CLJD model class do not perturb the principle topology of the fluid behavior at extreme conditions such that *Brown's* postulates for the characteristic curves are found to also apply to fluids with an elongation and polar interactions – even with large dipole moments. This holds for the independent predictions from both the computer experiment and the EOS results. Yet, there are some quantitative deviations (discussed in more detail below) between the results from the two methods. The fact that *Brown's* criteria

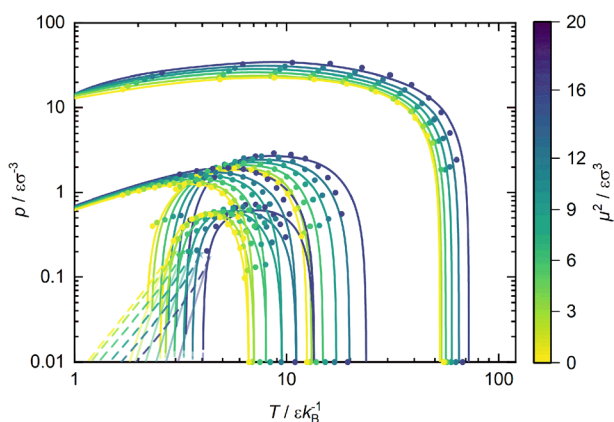


**Fig. 4** Characteristic curves of 2CLJD fluids with  $L/\sigma = 0.505$  and different  $\mu^2/\epsilon\sigma^3$  in the double-logarithmic  $p - T$ -projection. Results from computer experiments are represented by circles. Statistical uncertainties are within the symbol size. Lines represent the results from the EOS. Lines with 50% transparency indicate the vapor-liquid binodal (solid line) and spinodal (dashed line)

(intersection points, curvature etc. of characteristic curves) are applicable for molecules with significantly more complex interactions than simple dispersively interacting spherical molecules is probably due to the fact that the complex dipolar interactions have on average attractive and repulsive interaction effects. Hence, the applicability of *Brown's* criteria is likely related to the applicability of a mean field interaction picture. Hence, the directional orientation distribution present in polar fluids (as the 2CLJD fluid class) has no influence on the overall topology of *Brown's* characteristic curves.

Figures 5 and 6 show the results for the characteristic curves of the 2CLJD fluid for different elongations and dipole moments (cf. grey filled symbols in Fig. 2). Figure 5 shows the results for different elongations  $L$  at zero dipole moment  $\mu^2/\epsilon\sigma^3 = 0$ . Figure 6 shows the results for different dipole moments  $\mu^2$  at constant elongation  $L/\sigma = 0.505$ . The results are presented in the  $p - T$  and the  $\rho - T$  projection for each characteristic curve. The molecular simulation results are shown in comparison to the EOS results.

Considering the fact that the results from computer experiments and those from the EOS are independent predictions, they agree overall reasonably well. For the 2CLJD fluid with zero dipole moment, cf. Figure 5, the agreement of the results from the two methods is very good. For that case, the EOS (cf. Equation 13) comprises only the *Lisal et al.* [88] model. For these fluids, only some deviations between the results from the two methods are observed at high temperatures, e.g. for the Amagat curve, cf. Figure 5 c). Interestingly, these deviations are mostly observed for small  $L$ . The largest deviations between the EOS and the computer experiment results are observed for  $L = 0$ , which corresponds to the simple Lennard–Jones fluid. The *Lisal et al.* [88] EOS is a modification/ re-parametrization of the EOS proposed by *Mecke et al.* [95]. The latter, on the other hand, is known to yield some deviations at high temperatures [96], which are seemingly also present for the *Lisal* EOS for the simple Lennard–Jones fluid. For the 2CLJD fluids with (non-zero) dipole moment (cf. Figure 6), the EOS results show significant deviations from the computer experiment results. These deviations increase with increasing dipole moment. Since the 2CLJ results (no dipole moment) from the EOS agree very well with the computer experiment results, the deviations observed for the 2CLJD fluids (cf. Figure 6) can be attributed to the dipole EOS term. Yet, the qualitative effect of the dipole moment on the characteristic curves is correctly captured by the dipole EOS term.

The results provide interesting insights in the relation of the molecular interaction and molecular architecture parameters  $\mu$  and  $L$ , respectively, on the characteristic curves, cf. Figures 5 and 6. The two molecular parameters  $\mu$  and  $L$  have opposite effects on the characteristic curves. An increasing elongation  $L$  yields a monotonous decrease of both the characteristic curve pressure and density. An increasing dipole moment  $\mu$ , on the other hand, yields a monotonous increase of both the characteristic curve pressure and density. This is consistent to what was reported before for the vapor-liquid equilibrium coexisting density curves, vapor pressure curves [34], and surface tension [40] of the 2CLJD model class. The effect of  $L$  and  $\mu$  can be well understood from the microscopic level, i.e. with increasing  $L$ , the density of the mean dispersive interactions per unit volume decreases, which results for example in a decreasing critical temperature and Boyle temperature. For the dipole moment,

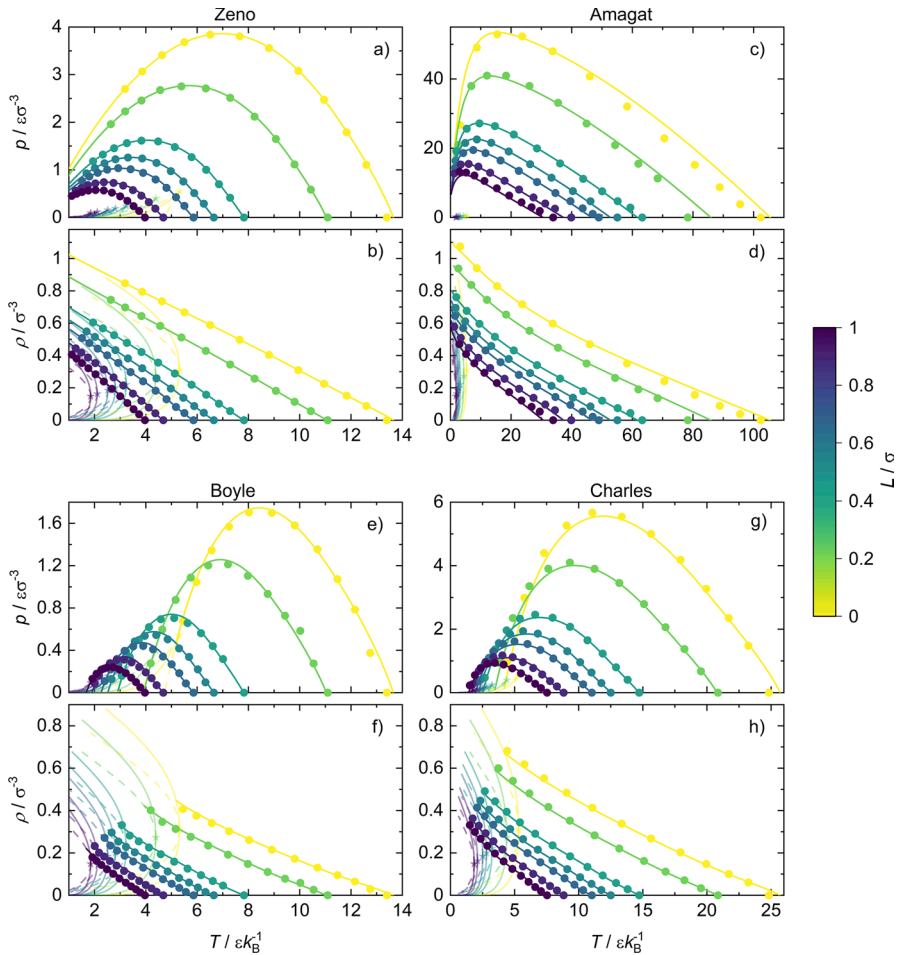


**Fig. 5** Characteristic curves of 2CLJ fluids with  $\mu^2/\varepsilon\sigma^3 = 0$  and different  $L/\sigma$ : a) and b) Zeno curve; c) and d) Amagat curve; e) and f) Boyle curve; g) and h) Charles curve. For all curves: Top plot is  $p - T$  projection and bottom plot is  $\rho - T$  projection. Results from MD simulations are represented by circles. Statistical uncertainties lie within the symbol size. Lines represent the EOS results. The 50% transparent lines and symbols indicate the vapor-liquid equilibrium (solid lines indicate binodal, dashed lines indicate spinodal, star indicates the critical point)

on the other hand, increasing  $\mu$  yields increasing mean attractive interactions due to the preferential orientation of the molecules caused by the anisotropy of the polar interactions.

In the studied  $L$  and  $\mu$  range, the elongation has a stronger influence on the characteristic curves compared to the dipole moment, cf. Figures 5 and 6. As expected, the elongation has in particular a more pronounced influence on the density of the characteristic curves (cf. Figure 5 b), d), f), h)) compared to the influence of the dipole moment (cf. Figure 6 b), d), f), h)). The differences of the influence of  $L$  and  $\mu$  on the characteristic curves can be seen well in the change of the pressure maximum

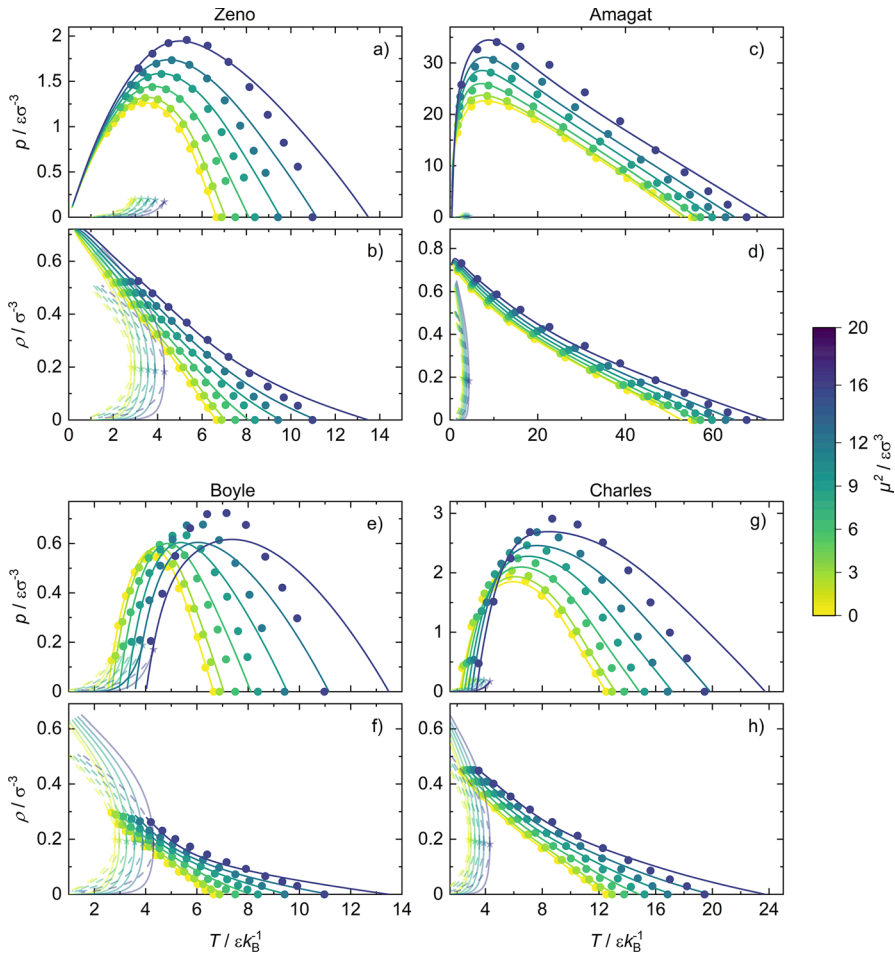


**Fig. 6** Characteristic curves of 2CLJD fluids with  $L/\sigma = 0.505$  and different  $\mu^2/\epsilon\sigma^3$ : a) and b) Zeno curve; c) and d) Amagat curve; e) and f) Boyle curve; g) and h) Charles curve. For all curves: Top plot is  $p - T$  projection and bottom plot is  $\rho - T$  projection. Results from MD simulations are represented by circles. Statistical uncertainties lie within the symbol size. Lines represent the EOS results. The 50% transparent lines and symbols indicate the vapor-liquid equilibrium (solid lines indicate binodal, dashed lines indicate spinodal, star indicates the critical point)

$p_{\max}$ . In the considered  $L$  range,  $p_{\max}$  undergoes four to eight fold changes. In contrast,  $p_{\max}$  changes only by a factor of about 1.5 in the studied dipole moment range.

For both molecular properties  $L$  and  $\mu$ , interesting differences are observed for the Zeno and Amagat curve on one hand and the Boyle and Charles curve on the other hand, cf. Figures 5 and 6. Considering the Zeno curve for the 2CLJD fluid with different  $\mu$ , cf. Figure 5 a). The pressure, temperature, and density are affected on the same order of magnitude, which holds for both the Zeno and the Amagat curve. Therefore, e.g. the Zeno curves do not intersect for different  $\mu$ . The same holds for the Amagat curves – for both the influence of  $L$  and  $\mu$ . For the Boyle and Charles

curve, on the other hand, the pressure, temperature, and density are affected differently by the dipole moment  $\mu$ , cf. Figure 5 e) for the Boyle curve. The same holds for the elongation  $L$ . The pressure of the Boyle curve is significantly less affected by the dipole moment than the temperature. The Boyle curves are mostly only shifted to higher temperatures with increasing  $\mu$ , which yields intersection points of the Boyle curves from different 2CLJD fluids in the vicinity of the pressure maximum. Similar findings are observed for the Charles curve, cf. Figure 5 g). Hence, the molecular interaction and architecture features have different effects for the different characteristic curves.

The  $\rho - T$  projection reveals an approximately linear trend for the Zeno curve, which has been extensively investigated by *Apfelbaum et al.* [97, 98]. The computer experiment results show an approximately linear shape for all studied 2CLJD fluids, cf. Figures 5 b) and 6 b) and the Supplementary Material. For the EOS results, some deviations from this linear behavior are observed with increasing dipole moment, cf. Figure 6 b), which can be attributed to the dipole term. Also the Amagat, Charles, and Boyle curve show in parts an approximately linear shape.

The quality of the molecular simulation results can be assessed by different measures. For all four characteristic curves, the MD simulation data (obtained in step (ii)) is in excellent agreement with the zero-density limit obtained from the virial route by MC simulations (obtained in step (i)). The zero-density limit data is overall more precise compared to the results obtained in step (ii), where a more complex evaluation has to be carried out [77]. Moreover, the simulation results for a given characteristic curve shows a smooth trend in all cases, cf. Figures 5 and 6.

Figure 7 shows the results for the Helmholtz energy consistency test [77] of the characteristic curve simulation results. The data used for evaluating the Helmholtz energy criteria are the results of the final MD simulation (step (iii)). Overall, the consistency test is satisfied for most data points – yet, some scattering is observed. The Helmholtz energy criteria is satisfied by 49% of the data points of the Zeno curve, 54% of the Amagat curve, 69% of the Boyle curve, and 63% of the Charles curve. Only very few data points are large outliers, cf. Figure 7. Systematic deviations are only observed for very low temperatures for the Amagat curve, where the state points possibly lie in the solid–fluid metastable region.

### 5.3 Corresponding States Principle

The principle of corresponding states formulates that substances share identical reduced states with respect to their critical properties [99, 100]. The principle of corresponding states was applied to thermophysical properties of the 2CLJD fluid previously in the literature. *Vega et al.* [50] studied the influence of the elongation and dipole moment on the second virial coefficient, *Lupkowski and Monson* [38], *Lisal et al.* [37], and *Stoll et al.* [34] applied this principle to vapor-liquid equilibrium properties.

According to the principle of corresponding states, for all 2CLJD fluids, each characteristic curve type – Zeno, Amagat, Boyle, and Charles – should fall on a single curve in a reduced projection. Figure 8 shows the molecular simulation



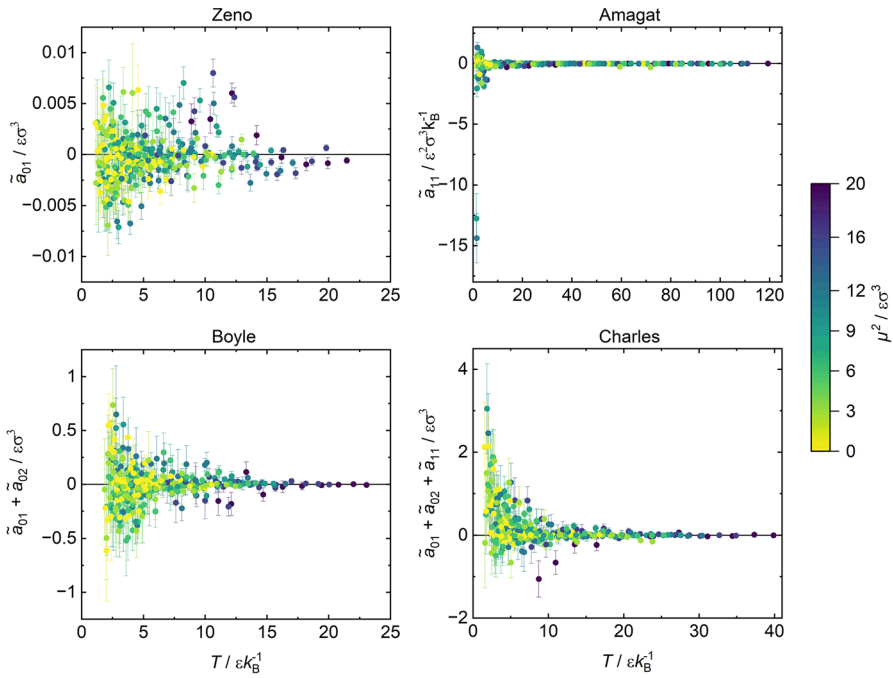


**Fig. 7** Results of thermodynamic consistency test of the Helmholtz energy criteria for the step (iii) simulation results. Results for all 43 studied 2CLJD fluids

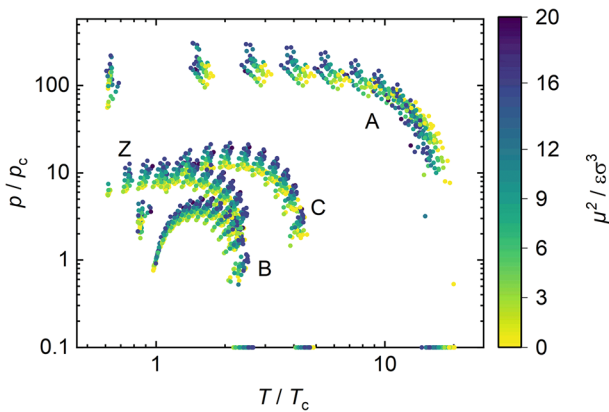


**Fig. 8** Characteristic curves of the 2CLJD fluids reduced by their corresponding critical properties. Critical point data is computed by the correlation of *Stoll et al.* [34]. Results for all studied 43 2CLJD fluids. The color code indicates the dipole moment

characteristic curve results in reduced units with respect to the critical point values for the respective 2CLJD fluid. The critical point properties were computed from the empirical correlation proposed by *Stoll et al.* [34].

Some deviations from the corresponding states principle are observed. For increasing dipole moment, the Boyle, Charles, and Zeno curve are shifted to higher pressures. For the Amagat curve, low temperature characteristic curve state points are also shifted to higher pressures, whereas for higher temperatures near the zero-density limit, the curve is shifted to lower pressures. With increasing elongation  $L$ , deviations from the principle of corresponding states are less pronounced compared to the influence of the dipole strength (see Supplementary Material).

#### 5.4 Intersection of Characteristic Curves and VLE

Figure 9 shows the results for the intersection points of the Charles and Boyle curves with the vapor-liquid equilibrium binodal and spinodal, respectively. Results are shown for the 2CLJD fluid with  $L/\sigma = 0.505$  and  $\mu^2/\varepsilon\sigma^3 = 6$ . Results

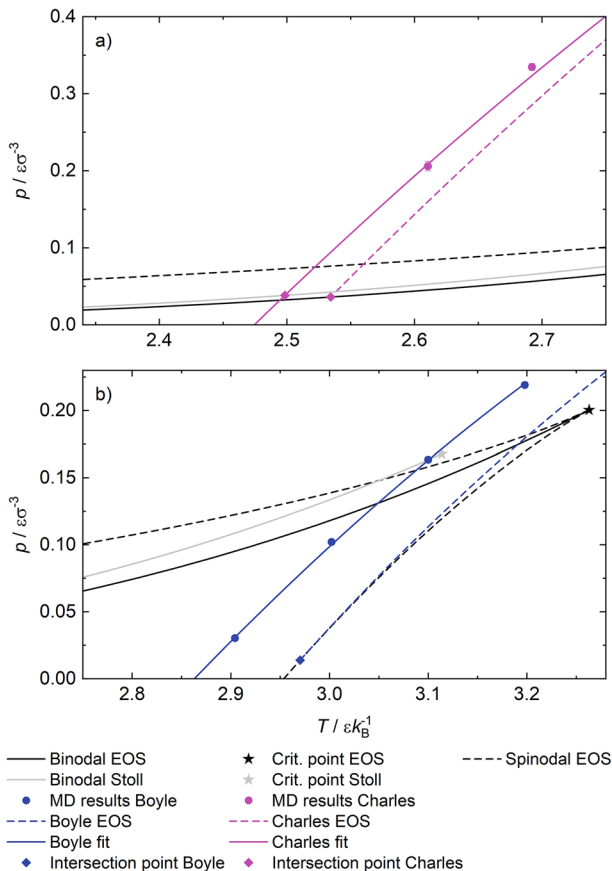


**Fig. 9** Characteristic curve intersection points: a) Charles curve with the binodal and b) Boyle curve with the spinodal. The results for the 2CLJD fluid with  $L/\sigma = 0.505$  and  $\mu^2/\varepsilon\sigma^3 = 6$  in the  $p - T$  projection. Results from the EOS, empirical correlations, and computer experiment – see legend. The binodal correlation model was taken from *Stoll et al.* [34]

are shown for both MD and EOS. For the EOS, the intersection points were determined solely from EOS results, i.e. both the characteristic curves and the binodal and spinodal were taken as predicted from the EOS defined by Eq. 13. For the MD results, an empirical fit of the characteristic curve data in the vicinity of the vapor-liquid equilibrium was used. In the case of the Charles curve, the empirical high accurate correlation of molecular simulation binodal data from Ref. [34] was used in conjunction with the MD characteristic curve results.

For both the Charles and the Boyle curve, cf. Figure 9 a) and b), respectively, significant deviations between the molecular simulation results and the EOS results are observed, which is mostly due to the fact that the critical point is overestimated by the EOS.

For the Boyle curve, characteristic curve state points were also determined in the metastable region, cf. Figure 9 b). Since the location of the spinodal has not yet been determined for the 2CLJD fluid, no intersection point was estimated for that case. In the case of the EOS results, the intersection point of the Boyle curve and the spinodal is interestingly located at approximately  $p = 0$ .

## 5.5 Application to Real Substances

The molecular simulation results were used to determine the parameters of the global empirical model for the four characteristic curves, cf. Equations 14–15. The obtained parameters are reported in the Appendix. For testing the applicability of the empirical characteristic curve model for the 2CLJD model class, the characteristic curves were evaluated for three real substance models, namely carbon monoxide (CO) and the refrigerants R152a ( $C_2H_4F_2$ ) and R134a ( $C_2H_2F_4$ ). The model parameters were taken from the MolMod database [8]. The models were originally developed for describing the vapor-liquid equilibrium of the fluids [15, 34]. The model parameters are given in Table 1.

The results are shown in Fig. 10. The characteristic curves obtained from the global empirical model are conform with *Brown's* criteria, e.g. no intersection of Amagat, Boyle, and Charles curve, negative curvature etc. Only for the CO Amagat curve result, a faint kink is observed.

**Table 1** Substance parameters of carbon monoxide (CO), R152a ( $C_2H_4F_2$ ), and R134a ( $C_2H_2F_4$ )

	$\sigma/\text{\AA}$	$\epsilon/k_B/K$	$L/\text{\AA}$	$\mu/D$	$L/\sigma$	$\mu^2/\epsilon\sigma^3$	Ref.
CO	3.3009	36.897	1.1405	0.7378	0.345512	2.971017	[34]
R152a	3.5168	182.010	3.3125	2.7354	0.941907	6.845726	[34]
R134a	3.819	140.4	2.5587	2.7491	0.670000	6.99993	[15]

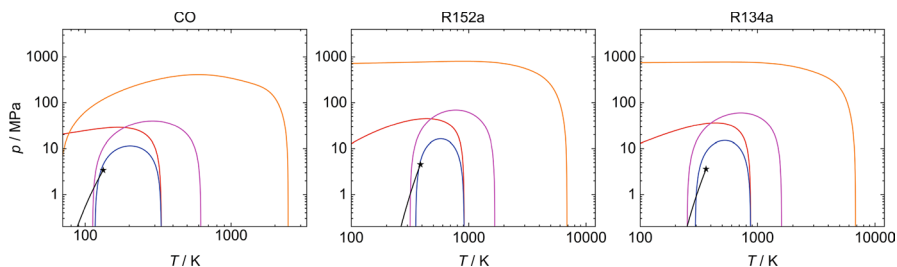


**Fig. 10** Characteristic curves in the  $p - T$  projection of CO (left), R152a (middle), and R134a (right). Results from the empirical correlation evaluated for the molecular models given in Table 1. Results for the Zeno (red), Amagat (orange), Boyle (blue), and Charles (pink) curve. Binodal (black) and critical point (star) were computed from the empirical correlation of *Stoll et al.* [34]

## 6 Conclusion

In this work, a systematic study on *Brown's* characteristic curves of the 2CLJD model fluid class was carried out for elucidating the influence of dipole interactions and the molecule elongation on the fluid behavior at extreme conditions. In total, 43 2CLJD model fluids were studied using molecular simulation and a molecular-based equation of state. Moreover, an empirical correlation for the characteristic curves was developed based on the molecular simulation results.

The topology of *Brown's* characteristic curves of a molecular fluid was originally derived for simple spherical molecules with repulsive and dispersive interactions. In this work, the topology of the characteristic curves of polar fluids was studied for the first time using first principle molecular simulations. It is thus shown that *Brown's* criteria for the topology of the characteristic curves apply not only for simple fluids, but can be transferred to molecules with more complex interactions. This indicates that a mean field picture is well applicable for the 2CLJD fluid, where the complex polar interactions can be considered as net attractive and repulsive interactions.

Interesting insights are obtained for the influence of the molecular parameters, i.e. the dipole moment  $\mu$  and the molecule elongation  $L$ , on the fluid behavior at extreme conditions. The characteristic curves become wider with increasing dipole moment and more narrow with increasing elongation. The influences on the characteristic curves can be well understood from the molecular interactions. Overall, the elongation has a surprisingly strong influence. The elongation has a more significant influence on the characteristic curves compared to the dipole moment. This is probably due to the fact that the fluid structure at extreme conditions is dominated by the shape of the molecule. Moreover, significant differences are observed for the behavior of the different characteristic curves of the 2CLJD model fluid class.

Additionally, the intersection points of the Charles and Boyle curve with the vapor-liquid equilibrium binodal and spinodal, respectively, were investigated. Especially for the Boyle curve, these simulations are challenging as the characteristic curve state points lie in the metastable region. Nevertheless, the simulation method proposed in Ref. [77] yields reliable results throughout.

New insights are also obtained on the performance of the employed molecular-based equation of state model. The EOS model for the 2CLJ fluid ( $\mu = 0$ ), i.e. the Helmholtz energy term proposed by *Lisal et al.* [88], describes the molecular simulation results very well. For the 2CLJD fluids ( $\mu > 0$ ), on the other hand, the EOS model yields systematic deviations to the molecular simulation results. Hence, these deviations are attributed to the dipole Helmholtz energy term (which was originally developed for describing VLE data). Nevertheless, the qualitative trends are accurately described by the 2CLJD EOS used in this work and, accordingly, capture the effect of  $L$  and  $\mu$  on the fluid behavior at extreme conditions.

## 7 Supplementary information

The molecular simulation data are provided in the electronic Supplementary Information in a spreadsheet file.

## Parameters of Empirical Correlation

The model parameters  $d_i$  and  $f_i$  for the empirical characteristic curve models for the 2CLJD fluids, cf. Equations 14 and 15 are given in Tables 2 and 3. Table 2 reports the parameter values for the zero-density limit characteristic point function. Table 3

**Table 2** Parameters  $d_i$  and  $f_i$  for the empirical correlation (15) for the temperature  $T_{\text{char},i}$  of the zero-density characteristic points of the 2CLJD fluid class

	$T_{\text{char,Amagat}}/\epsilon k_{\text{B}}^{-1}$	$T_{\text{char,Boyle}}/\epsilon k_{\text{B}}^{-1}$	$T_{\text{char,Charles}}/\epsilon k_{\text{B}}^{-1}$
$d_1$	$1.0216399735 \cdot 10^2$	$1.3387256938 \cdot 10^1$	$2.4850772265 \cdot 10^1$
$d_2$	$-1.4491443421 \cdot 10^2$	$-4.9446410831$	$-7.8995977905$
$d_3$	$1.6020912352 \cdot 10^2$	$-4.7018819823 \cdot 10^1$	$-9.0018256784 \cdot 10^1$
$d_4$	$-1.4113695816 \cdot 10^2$	$7.8305962800 \cdot 10^1$	$1.4713716011 \cdot 10^2$
$d_5$	$5.7656349728 \cdot 10^1$	$-3.5780808747 \cdot 10^1$	$-6.6620269050 \cdot 10^1$
$f_1$	$2.9348000318 \cdot 10^{-2}$	$3.3639976641 \cdot 10^{-3}$	$2.9719945706 \cdot 10^{-3}$
$f_2$	$-3.7093316614 \cdot 10^{-1}$	$-1.7900152118 \cdot 10^{-1}$	$-2.0453238321 \cdot 10^{-1}$
$f_3$	$-2.4288631166 \cdot 10^{-1}$	$1.5063522747 \cdot 10^{-1}$	$1.7289622439 \cdot 10^{-1}$
$f_4$	$1.2081427572 \cdot 10^{-1}$	$4.2617299813 \cdot 10^{-2}$	$6.7983482295 \cdot 10^{-2}$
$f_5$	$-1.1255598782 \cdot 10^{-1}$	$2.3421359861 \cdot 10^{-3}$	$-1.9887545552 \cdot 10^{-2}$
$f_6$	$2.9400091183 \cdot 10^{-1}$	$-1.3496460934 \cdot 10^{-2}$	$-6.2019144729 \cdot 10^{-3}$
$f_7$	$-2.2261306434 \cdot 10^{-3}$	$-8.7161786706 \cdot 10^{-4}$	$-1.4612528486 \cdot 10^{-3}$
$f_8$	$6.2713071723 \cdot 10^{-4}$	$-2.6645218072 \cdot 10^{-3}$	$-2.2334861947 \cdot 10^{-3}$
$f_9$	$-2.8248741543 \cdot 10^{-2}$	$1.2098826769 \cdot 10^{-3}$	$1.0547108535 \cdot 10^{-3}$
$f_{10}$	$4.1981844512 \cdot 10^{-5}$	$4.0549307175 \cdot 10^{-6}$	$1.3308568735 \cdot 10^{-5}$
$f_{11}$	$-5.7533844690 \cdot 10^{-5}$	$7.3077386679 \cdot 10^{-5}$	$5.7615748071 \cdot 10^{-5}$
$f_{12}$	$9.6734591063 \cdot 10^{-4}$	$-5.8809378238 \cdot 10^{-6}$	$5.1596632402 \cdot 10^{-6}$

**Table 3** Parameter values for  $d_i$  and  $f_i$  for the parameters  $a$ – $e$  of the correlation for the reduced characteristic curves for the 2CLJD fluid class in  $p - T$  projection, using Eqs. 14 and 15

	$a$	$b$	$l$	$d$	$e$
Zeno					
$d_1$	$2.3605552 \cdot 10^5$	$7.6084834 \cdot 10^3$	$-3.6749303 \cdot 10^1$	$-8.3589781 \cdot 10^5$	$-1.5248228 \cdot 10^6$
$d_2$	$-1.0940337 \cdot 10^6$	$-3.6860614 \cdot 10^4$	$2.1611845 \cdot 10^1$	$3.5554720 \cdot 10^6$	$7.3850643 \cdot 10^6$
$d_3$	$2.5367791 \cdot 10^6$	$8.4726539 \cdot 10^4$	$-1.2202270 \cdot 10^2$	$-8.3957290 \cdot 10^6$	$-1.6972057 \cdot 10^7$
$d_4$	$-2.1466960 \cdot 10^6$	$-6.8988119 \cdot 10^4$	$3.6580505 \cdot 10^2$	$7.6524230 \cdot 10^6$	$1.3813798 \cdot 10^7$
$d_5$	$7.5011107 \cdot 10^5$	$2.3101111 \cdot 10^4$	$-2.2494867 \cdot 10^2$	$-2.8772046 \cdot 10^6$	$-4.6233799 \cdot 10^6$
$f_1$	$1.0248440 \cdot 10^4$	$3.5754578 \cdot 10^2$	$9.7270293 \cdot 10^{-1}$	$-3.0878782 \cdot 10^4$	$-7.1597856 \cdot 10^4$
$f_2$	$-2.7222501 \cdot 10^4$	$-8.7391838 \cdot 10^2$	$3.6512289$	$9.8124031 \cdot 10^4$	$1.7397880 \cdot 10^5$
$f_3$	$3.7546207 \cdot 10^4$	$1.2009676 \cdot 10^3$	$-5.9385818$	$-1.3571081 \cdot 10^5$	$-2.3962313 \cdot 10^5$
$f_4$	$1.3219434 \cdot 10^3$	$4.3216952 \cdot 10^1$	$-1.5473088 \cdot 10^{-1}$	$-4.5427528 \cdot 10^3$	$-8.6801867 \cdot 10^3$
$f_5$	$-7.7708613 \cdot 10^3$	$-2.5765349 \cdot 10^2$	$7.0796216 \cdot 10^{-1}$	$2.5958925 \cdot 10^4$	$5.1783393 \cdot 10^4$
$f_6$	$-1.0713924 \cdot 10^3$	$-3.9612761 \cdot 10^1$	$-4.4306725 \cdot 10^{-1}$	$2.8535817 \cdot 10^3$	$7.8258967 \cdot 10^3$
$f_7$	$-5.4166007 \cdot 10^1$	$-1.6201090$	$2.1487924 \cdot 10^{-2}$	$2.1553915 \cdot 10^2$	$3.2636569 \cdot 10^2$
$f_8$	$8.9042684 \cdot 10^2$	$2.9419875 \cdot 10^1$	$-8.2458230 \cdot 10^{-2}$	$-3.0058052 \cdot 10^3$	$-5.9013753 \cdot 10^3$
$f_9$	$9.5794225 \cdot 10^1$	$3.7493574$	$5.4396659 \cdot 10^{-2}$	$-2.0554918 \cdot 10^2$	$-7.4940641 \cdot 10^2$
$f_{10}$	$3.4338622 \cdot 10^{-1}$	$1.4009375 \cdot 10^{-3}$	$-1.0076745 \cdot 10^{-3}$	$-3.1216386$	$-3.1740818 \cdot 10^{-1}$
$f_{11}$	$-3.2669945 \cdot 10^1$	$-1.0776073$	$2.9988882 \cdot 10^{-3}$	$1.1084988 \cdot 10^2$	$2.1593163 \cdot 10^2$
$f_{12}$	$1.2281066$	$2.2725957 \cdot 10^{-2}$	$-1.8524104 \cdot 10^{-3}$	$-7.9515550$	$-4.4140577$
Amagat					
$d_1$	$1.3299841 \cdot 10^3$	$5.4541500 \cdot 10^1$	$8.5851255 \cdot 10^{-1}$	$-2.7253493 \cdot 10^3$	$-1.0606041 \cdot 10^4$
$d_2$	$3.2308280 \cdot 10^4$	$1.3760601 \cdot 10^3$	$2.4533996 \cdot 10^1$	$-3.6364425 \cdot 10^4$	$-2.8890848 \cdot 10^5$
$d_3$	$-1.1784931 \cdot 10^5$	$-5.0736498 \cdot 10^3$	$-9.2735164 \cdot 10^1$	$1.0397414 \cdot 10^5$	$1.0854647 \cdot 10^6$
$d_4$	$1.5020345 \cdot 10^5$	$6.5013770 \cdot 10^3$	$1.2025184 \cdot 10^2$	$-1.1420282 \cdot 10^5$	$-1.4039314 \cdot 10^6$
$d_5$	$-6.3597645 \cdot 10^4$	$-2.7576727 \cdot 10^3$	$-5.1211930 \cdot 10^1$	$4.6131921 \cdot 10^4$	$5.9702743 \cdot 10^5$
$f_1$	$2.3512739 \cdot 10^2$	$9.6184514$	$1.5329725 \cdot 10^{-1}$	$-8.0330564 \cdot 10^2$	$-1.4665988 \cdot 10^3$
$f_2$	$-2.4656222 \cdot 10^2$	$-6.5284227$	$3.8282364 \cdot 10^{-2}$	$3.5154757 \cdot 10^3$	$-1.4617129 \cdot 10^3$
$f_3$	$1.8019327 \cdot 10^1$	$-3.8707183$	$-2.4155430 \cdot 10^{-1}$	$-3.2464979 \cdot 10^3$	$3.4320995 \cdot 10^3$
$f_4$	$-8.7942095$	$-3.5494077 \cdot 10^{-1}$	$-5.5218874 \cdot 10^{-3}$	$1.0684045 \cdot 10^2$	$-3.8687089 \cdot 10^1$
$f_5$	$-2.0605723 \cdot 10^2$	$-8.8599631$	$-1.5848258 \cdot 10^{-1}$	$-9.2406802 \cdot 10^1$	$2.2245122 \cdot 10^3$
$f_6$	$1.2635061 \cdot 10^2$	$5.6809922$	$1.0926341 \cdot 10^{-1}$	$1.6711907 \cdot 10^2$	$-1.4782397 \cdot 10^3$
$f_7$	$4.8509115$	$2.0672755 \cdot 10^{-1}$	$3.6770772 \cdot 10^{-3}$	$-1.3130915 \cdot 10^1$	$-3.3960634 \cdot 10^1$
$f_8$	$1.6622833 \cdot 10^1$	$6.8443903 \cdot 10^{-1}$	$1.0982816 \cdot 10^{-2}$	$-7.8551255$	$-1.6282401 \cdot 10^2$
$f_9$	$-1.0657795 \cdot 10^1$	$-4.3990313 \cdot 10^{-1}$	$-6.9210236 \cdot 10^{-3}$	$7.0318936$	$1.0146632 \cdot 10^2$
$f_{10}$	$-2.2882077 \cdot 10^{-1}$	$-9.7570333 \cdot 10^{-3}$	$-1.7355066 \cdot 10^{-4}$	$4.5498402 \cdot 10^{-1}$	$1.8018148$
$f_{11}$	$-3.5283217 \cdot 10^{-1}$	$-1.3988659 \cdot 10^{-2}$	$-1.9977553 \cdot 10^{-4}$	$3.5924830 \cdot 10^{-1}$	$3.2566560$
$f_{12}$	$2.4497215 \cdot 10^{-1}$	$9.4802899 \cdot 10^{-3}$	$1.2051702 \cdot 10^{-4}$	$-4.7590445 \cdot 10^{-1}$	$-1.9867411$
Boyle					
$d_1$	$3.6881508 \cdot 10^4$	$1.7881801 \cdot 10^3$	$5.2835882 \cdot 10^1$	$-1.0007763 \cdot 10^4$	$-3.5888347 \cdot 10^5$
$d_2$	$1.2464572 \cdot 10^5$	$6.0332583 \cdot 10^3$	$1.7884732 \cdot 10^2$	$-3.9978028 \cdot 10^4$	$-1.2064586 \cdot 10^6$
$d_3$	$-4.3982462 \cdot 10^5$	$-2.7267191 \cdot 10^4$	$-1.2009640 \cdot 10^3$	$-1.0630719 \cdot 10^6$	$5.4615393 \cdot 10^6$
$d_4$	$5.1580743 \cdot 10^5$	$3.7815972 \cdot 10^4$	$1.9733232 \cdot 10^3$	$2.4195378 \cdot 10^6$	$-7.5781357 \cdot 10^6$
$d_5$	$-1.8571405 \cdot 10^5$	$-1.6177321 \cdot 10^4$	$-9.5799879 \cdot 10^2$	$-1.3855104 \cdot 10^6$	$3.2429513 \cdot 10^6$

**Table 3** (continued)

	<i>a</i>	<i>b</i>	<i>l</i>	<i>d</i>	<i>e</i>
$f_1$	$5.2734838 \cdot 10^3$	$2.7500974 \cdot 10^2$	9.2721369	$2.4062103 \cdot 10^3$	$-5.5141892 \cdot 10^4$
$f_2$	$-9.6725462 \cdot 10^3$	$-5.8877418 \cdot 10^2$	$-2.4560859 \cdot 10^1$	$-2.1235119 \cdot 10^4$	$1.1795068 \cdot 10^5$
$f_3$	$1.1477286 \cdot 10^4$	$6.5931523 \cdot 10^2$	$2.5172800 \cdot 10^1$	$1.7433024 \cdot 10^4$	$-1.3219805 \cdot 10^5$
$f_4$	$-8.5129621 \cdot 10^2$	$-4.4114996 \cdot 10^1$	-1.4314891	$-3.3891353 \cdot 10^2$	$8.8517607 \cdot 10^3$
$f_5$	$3.0195535 \cdot 10^3$	$1.7419182 \cdot 10^2$	6.7645756	$4.6995953 \cdot 10^3$	$-3.4892945 \cdot 10^4$
$f_6$	$-4.4772488 \cdot 10^3$	$-2.4391086 \cdot 10^2$	-8.6487877	$-4.1283872 \cdot 10^3$	$4.8899759 \cdot 10^4$
$f_7$	$7.1287875 \cdot 10^1$	3.1717538	$6.8544872 \cdot 10^{-2}$	$-7.6044346 \cdot 10^1$	$-6.3684149 \cdot 10^2$
$f_8$	$-3.7462487 \cdot 10^2$	$-1.9171275 \cdot 10^1$	$-6.1346471 \cdot 10^{-1}$	$-9.4557615 \cdot 10^1$	$3.8407138 \cdot 10^3$
$f_9$	$5.4221076 \cdot 10^2$	$2.7701682 \cdot 10^1$	$8.8094262 \cdot 10^{-1}$	$1.3165780 \cdot 10^2$	$-5.5537932 \cdot 10^3$
$f_{10}$	-2.0530383	$-8.2366939 \cdot 10^{-2}$	$-1.1102814 \cdot 10^{-3}$	3.9861590	$1.6544864 \cdot 10^1$
$f_{11}$	$1.2332061 \cdot 10^1$	$6.0149828 \cdot 10^{-1}$	$1.7495787 \cdot 10^{-2}$	-2.8079890	$-1.2051206 \cdot 10^2$
$f_{12}$	$-1.7477666 \cdot 10^1$	$-8.6980425 \cdot 10^{-1}$	$-2.6327017 \cdot 10^{-2}$	$3.8274350 \cdot 10^{-1}$	$1.7439747 \cdot 10^2$
Charles					
$d_1$	$8.1333280 \cdot 10^3$	$4.0371092 \cdot 10^2$	$1.1868915 \cdot 10^1$	$2.9711983 \cdot 10^2$	$-8.1737897 \cdot 10^4$
$d_2$	$-5.0070445 \cdot 10^4$	$-2.1285447 \cdot 10^3$	$-3.8438923 \cdot 10^1$	$6.9975382 \cdot 10^4$	$4.3094569 \cdot 10^5$
$d_3$	$1.2203638 \cdot 10^5$	$5.1170057 \cdot 10^3$	$8.6660691 \cdot 10^1$	$-1.8420720 \cdot 10^5$	$-1.0364918 \cdot 10^6$
$d_4$	$-1.2874527 \cdot 10^5$	$-5.0338430 \cdot 10^3$	$-5.6296623 \cdot 10^1$	$2.6735851 \cdot 10^5$	$1.0201087 \cdot 10^6$
$d_5$	$4.8424519 \cdot 10^4$	$1.7916869 \cdot 10^3$	$1.1324035 \cdot 10^1$	$-1.2087389 \cdot 10^5$	$-3.6324222 \cdot 10^5$
$f_1$	$-9.7108897 \cdot 10^1$	-3.0309296	$2.8618085 \cdot 10^{-2}$	$3.5924030 \cdot 10^2$	$6.1392171 \cdot 10^2$
$f_2$	$2.5678644 \cdot 10^2$	$3.9409156 \cdot 10^1$	2.7887098	$5.5385808 \cdot 10^3$	$-8.1229139 \cdot 10^3$
$f_3$	$-1.6906277 \cdot 10^2$	$-2.5393186 \cdot 10^1$	-1.7438511	$-3.5677276 \cdot 10^3$	$5.2721330 \cdot 10^3$
$f_4$	$1.3827291 \cdot 10^2$	6.2702438	$1.5355676 \cdot 10^{-1}$	$-1.2577828 \cdot 10^2$	$-1.2577118 \cdot 10^3$
$f_5$	$-5.2376022 \cdot 10^2$	$-2.4956017 \cdot 10^1$	$-6.5660745 \cdot 10^{-1}$	$2.0395161 \cdot 10^2$	$5.0353438 \cdot 10^3$
$f_6$	$4.1032951 \cdot 10^2$	$1.6221941 \cdot 10^1$	$2.0239449 \cdot 10^{-1}$	$-8.4477923 \cdot 10^2$	$-3.2586735 \cdot 10^3$
$f_7$	$-1.5647049 \cdot 10^1$	$-7.0482575 \cdot 10^{-1}$	$-1.6624376 \cdot 10^{-2}$	$1.5202281 \cdot 10^1$	$1.4129637 \cdot 10^2$
$f_8$	$5.8392742 \cdot 10^1$	2.3870077	$3.6285767 \cdot 10^{-2}$	$-1.0423972 \cdot 10^2$	$-4.7965350 \cdot 10^2$
$f_9$	$-4.5383462 \cdot 10^1$	-1.3157174	$2.1513704 \cdot 10^{-2}$	$1.9244443 \cdot 10^2$	$2.6114007 \cdot 10^2$
$f_{10}$	$4.2730840 \cdot 10^{-1}$	$1.8900545 \cdot 10^{-2}$	$4.1897510 \cdot 10^{-4}$	$-4.8807162 \cdot 10^{-1}$	-3.7850024
$f_{11}$	-1.5905368	$-5.8065542 \cdot 10^{-2}$	$-3.3998427 \cdot 10^{-4}$	4.2763853	$1.1624475 \cdot 10^1$
$f_{12}$	1.2345835	$2.4050176 \cdot 10^{-2}$	$-1.6644278 \cdot 10^{-3}$	-7.6673785	-4.6657590

reports the parameter values for the reduced pressure  $p^*$  function describing the characteristic curves.

**Supplementary Information** The online version contains supplementary material available at <https://doi.org/10.1007/s10765-024-03366-8>.

**Acknowledgements** We gratefully acknowledge fruitful discussions with U.K. Deiters. The simulations were carried out on the HPC machine ELWE at the RHRZ under the grant RPTU-MTD and on the HPC machine MOGON at the NHR SW under the grant TU-MSG (supported by the Federal Ministry of Education and Research and the state governments).

**Author Contributions** H. Renneis: Data curation, formal analysis, visualisation, and writing/original draft preparation (support); S. Stephan.: conceptualization, methodology, supervision, writing/original draft preparation (lead), and funding acquisition.

**Funding** Open Access funding enabled and organized by Projekt DEAL. We gratefully acknowledge funding from the European Union's Horizon Europe research and innovation programme under grant agreement no. 101137725 (BatCAT).

**Data Availability Statement** Data is provided within the manuscript or supplementary information files

## Declarations

**Conflict of interest** The authors have no Conflict of interest to declare.

**Open Access** This article is licensed under a Creative Commons Attribution 4.0 International License, which permits use, sharing, adaptation, distribution and reproduction in any medium or format, as long as you give appropriate credit to the original author(s) and the source, provide a link to the Creative Commons licence, and indicate if changes were made. The images or other third party material in this article are included in the article's Creative Commons licence, unless indicated otherwise in a credit line to the material. If material is not included in the article's Creative Commons licence and your intended use is not permitted by statutory regulation or exceeds the permitted use, you will need to obtain permission directly from the copyright holder. To view a copy of this licence, visit <http://creativecommons.org/licenses/by/4.0/>.

## References

1. C.G. Gray, K.E. Gubbins, *Theory of Molecular Fluids. Fundamentals*, vol. 1 (Clarendon Press, Oxford, 1984)
2. J. Tomasi, B. Mennucci, R. Cammi, Quantum mechanical continuum solvation models. *Chem. Rev.* **105**, 2999–3094 (2005). <https://doi.org/10.1021/cr9904009>
3. S. Deublein, B. Eckl, J. Stoll, S.V. Lishchuk, G. Guevara-Carrion, C.W. Glass, T. Merker, M. Bernreuther, H. Hasse, J. Vrabec, ms2: A molecular simulation tool for thermodynamic properties. *Comput. Phys. Commun.* **182**, 2350–2367 (2011). <https://doi.org/10.1016/j.cpc.2011.04.026>
4. A.J. Stone, Intermolecular potentials. *Science* **321**, 787–789 (2008). <https://doi.org/10.1126/science.1158006>
5. J. Stoll, J. Vrabec, H. Hasse, A set of molecular models for carbon monoxide and halogenated hydrocarbons. *J. Chem. Phys.* **119**, 11396–11407 (2003). <https://doi.org/10.1063/1.1623475>
6. M.E. van Leeuwen, Derivation of Stockmayer potential parameters for polar fluids. *Fluid Phase Equilib.* **99**, 1–18 (1994). [https://doi.org/10.1016/0378-3812\(94\)80018-9](https://doi.org/10.1016/0378-3812(94)80018-9)
7. J. Gao, W.D. Luedtke, U. Landman, Layering transitions and dynamics of confined liquid films. *Phys. Rev. Lett.* **79**, 705–708 (1997). <https://doi.org/10.1103/physrevlett.79.705>
8. S. Stephan, M. Horsch, J. Vrabec, H. Hasse, MolMod—an open access database of force fields for molecular simulations of fluids. *Mol. Simul.* **45**, 806–814 (2019). <https://doi.org/10.1080/08927022.2019.1601191>
9. S. Schmitt, G. Kanagalingam, F. Fleckenstein, D. Froescher, H. Hasse, S. Stephan, Extension of the MolMod database to transferable force fields. *J. Chem. Inf. Model.* **63**, 7148–7158 (2023). <https://doi.org/10.1021/acs.jcim.3c01484>
10. O.C. Madin, S. Boothroyd, R.A. MESSERLY, J. Fass, J.D. Chodera, M.R. Shirts, Bayesian-inference-driven model parametrization and model selection for 2CLJQ fluid models. *J. Chem. Inf. Model.* **62**, 874–889 (2022). <https://doi.org/10.1021/acs.jcim.1c00829>
11. K. Stöbener, P. Klein, M. Horsch, K. Küfer, H. Hasse, Parametrization of two-center Lennard-Jones plus point-quadrupole force field models by multicriteria optimization. *Fluid Phase Equilib.* **411**, 33–42 (2016). <https://doi.org/10.1016/j.fluid.2015.11.028>



12. R. Span, W. Wagner, Equations of state for technical applications. III. Results for polar fluids. *Int. J. Thermophys.* **24**, 111–162 (2003). <https://doi.org/10.1023/A:1022362231796>
13. T. Merker, C. Engin, J. Vrabec, H. Hasse, Molecular model for carbon dioxide optimized to vapor-liquid equilibria. *J. Chem. Phys.* **132**, 234512 (2010). <https://doi.org/10.1063/1.3434530>
14. C. Vega, B. Saager, J. Fischer, Molecular dynamics studies for the new refrigerant R152a with simple model potentials. *Mol. Phys.* **68**, 1079–1093 (1989). <https://doi.org/10.1080/00268978900102751>
15. M. Lísal, R. Budinský, V. Vacek, K. Aim, Vapor-liquid equilibria of alternative refrigerants by molecular dynamics simulations. *Int. J. Thermophys.* **20**, 163–174 (1999). <https://doi.org/10.1023/A:1021490500152>
16. C. Kriebel, M. Mecke, J. Winkelmann, J. Vrabec, J. Fischer, An equation of state for dipolar two-center Lennard-Jones molecules and its application to refrigerants. *Fluid Phase Equilib.* **142**, 15–32 (1998). [https://doi.org/10.1016/S0378-3812\(97\)00291-4](https://doi.org/10.1016/S0378-3812(97)00291-4)
17. J. Gross, J. Vrabec, An equation-of-state contribution for polar components: dipolar molecules. *AIChE J.* **52**, 1194–1204 (2006). <https://doi.org/10.1002/aic.10683>
18. W.G. Chapman, Prediction of the thermodynamic properties of associating Lennard-Jones fluids: theory and simulation. *J. Chem. Phys.* **93**, 4299–4304 (1990). <https://doi.org/10.1063/1.458711>
19. A.E. Nasrabad, R. Laghaei, B.C. Eu, Molecular theory of thermal conductivity of the Lennard-Jones fluid. *J. Chem. Phys.* **124**, 084506 (2006). <https://doi.org/10.1063/1.2166394>
20. D. Fertig, H. Hasse, S. Stephan, Transport properties of binary Lennard-Jones mixtures: Insights from entropy scaling and conformal solution theory. *J. Mol. Liq.* **367**, 120401 (2022). <https://doi.org/10.1016/j.molliq.2022.120401>
21. F.J. Blas, L.F. Vega, Thermodynamic behaviour of homonuclear and heteronuclear Lennard-Jones chains with association sites from simulation and theory. *Mol. Phys.* **92**, 135–150 (1997). <https://doi.org/10.1080/002689797170707>
22. K. Langenbach, M. Kohns, Relative permittivity of dipolar model fluids from molecular simulation and from the co-oriented fluid functional equation for electrostatic interactions. *J. Chem. Eng. Data* **65**, 980–986 (2019). <https://doi.org/10.1021/acs.jced.9b00296>
23. J. Lenhard, S. Stephan, H. Hasse, A child of prediction. on the history, ontology, and computation of the Lennard-Jonesium. *Stud. Hist. Philos. Sci.* **103**, 105–113 (2024). <https://doi.org/10.1016/j.shpsa.2023.11.007>
24. S. Stephan, K. Langenbach, H. Hasse, Interfacial properties of binary Lennard-Jones mixtures by molecular simulations and density gradient theory. *J. Chem. Phys.* **150**, 174704 (2019). <https://doi.org/10.1063/1.5093603>
25. S.P. Protsenko, V.G. Baidakov, V.M. Bryukhanov, Binary Lennard-Jones mixtures with highly asymmetric interactions of the components. 2. effect of the particle size on phase equilibria and properties of liquid-gas interfaces. *Fluid Phase Equilib.* **430**, 67–74 (2016). <https://doi.org/10.1016/j.fluid.2016.09.022>
26. S.P. Protsenko, V.G. Baidakov, Binary Lennard-Jones mixtures with highly asymmetric interactions of the components. 1. Effect of the energy parameters on phase equilibria and properties of liquid-gas interfaces. *Fluid Phase Equilib.* **429**, 242–253 (2016). <https://doi.org/10.1016/j.fluid.2016.09.009>
27. I. Antolović, J. Staubach, S. Stephan, J. Vrabec, Phase equilibria of symmetric Lennard-Jones mixtures and a look at the transport properties near the upper critical solution temperature. *Phys. Chem. Chem. Phys.* **25**, 17627–17638 (2023). <https://doi.org/10.1039/d3cp01434g>
28. S. Stephan, H. Hasse, Molecular interactions at vapor-liquid interfaces: binary mixtures of simple fluids. *Phys. Rev. E* **101**, 012802 (2020). <https://doi.org/10.1103/PhysRevE.101.012802>
29. E.L. Granados-Bazán, S.E. Quiñones-Cisneros, U.K. Deiters, Interfacial properties of binary mixtures of Lennard-Jones chains in planar interfaces by molecular dynamics simulation. *J. Chem. Phys.* **154**, 084704 (2021). <https://doi.org/10.1063/5.0042340>
30. F.J. Martinez-Ruiz, F.J. Blas, Interfacial properties of binary mixtures of square-well molecules from Monte Carlo simulation. *J. Chem. Phys.* **144**, 154705 (2016). <https://doi.org/10.1063/1.4947017>
31. S. Enders, H. Kahl, M. Mecke, J. Winkelmann, Molecular dynamics simulation of the liquid-vapor interface: I. the orientational profile of 2-center Lennard-Jones and of Stockmayer fluid molecules. *J. Mol. Liq.* **115**, 29–39 (2004). <https://doi.org/10.1016/j.molliq.2003.12.020>

32. S. Stephan, M. Thol, J. Vrabec, H. Hasse, Thermophysical properties of the Lennard-Jones fluid: Database and data assessment. *J. Chem. Inf. Model.* **59**, 4248–4265 (2019). <https://doi.org/10.1021/acs.jcim.9b00620>
33. J. Stoll, J. Vrabec, H. Hasse, J. Fischer, Comprehensive study of the vapour-liquid equilibria of the pure two-centre Lennard-Jones plus pointquadrupole fluid. *Fluid Phase Equilib.* **179**, 339–362 (2001). [https://doi.org/10.1016/S0378-3812\(00\)00506-9](https://doi.org/10.1016/S0378-3812(00)00506-9)
34. J. Stoll, J. Vrabec, H. Hasse, Comprehensive study of the vapour-liquid equilibria of the pure two-centre Lennard-Jones plus pointdipole fluid. *Fluid Phase Equilib.* **209**, 29–53 (2003). [https://doi.org/10.1016/S0378-3812\(03\)00074-8](https://doi.org/10.1016/S0378-3812(03)00074-8)
35. J. Vrabec, J. Stoll, H. Hasse, A set of molecular models for symmetric quadrupolar fluids. *J. Phys. Chem. B* **105**, 12126–12133 (2001). <https://doi.org/10.1021/jp012542o>
36. C. Kriebel, A. Müller, J. Winkelmann, J. Fischer, Vapour-liquid equilibria of two-centre Lennard-Jones fluids from the NpT plus test particle method. *Mol. Phys.* **84**, 381–394 (1995). <https://doi.org/10.1080/00268979500100261>
37. M. Lísal, R. Budinský, V. Vacek, Vapour-liquid equilibria for dipolar two-centre Lennard-Jones fluids by Gibbs-Duhem integration. *Fluid Phase Equilib.* **135**, 193–207 (1997). [https://doi.org/10.1016/S0378-3812\(97\)00072-1](https://doi.org/10.1016/S0378-3812(97)00072-1)
38. M. Lupkowski, P.A. Monson, Phase diagrams of interaction site fluids. *Mol. Phys.* **67**, 53–66 (1989). <https://doi.org/10.1080/00268978900100921>
39. S. Werth, M. Horsch, H. Hasse, Surface tension of the two center Lennard-Jones plus quadrupole model fluid. *Fluid Phase Equilib.* **392**, 12–18 (2015). <https://doi.org/10.1016/j.fluid.2015.02.003>
40. S. Werth, M. Horsch, H. Hasse, Surface tension of the two center Lennard-Jones plus point dipole fluid. *J. Chem. Phys.* **144**, 054702 (2016). <https://doi.org/10.1063/1.4940966>
41. V.B. Warshavsky, X.C. Zeng, Fundamental measure density functional theory study of liquid-vapor interface of dipolar and quadrupolar fluids. *J. Chem. Phys.* **139**, 134502 (2013). <https://doi.org/10.1063/1.4822325>
42. V.B. Warshavsky, X.C. Zeng, Bulk and interfacial properties of quadrupolar fluids. *J. Chem. Phys.* **117**, 3982–3991 (2002). <https://doi.org/10.1063/1.1495841>
43. B. Smit, C.P. Williams, Vapour-liquid equilibria for quadrupolar Lennard-Jones fluids. *J. Phys. Condens. Matter* **2**, 4281 (1990)
44. J.H. Pérez-López, J.E. Puig, M.A. Leiva, Gradient theory of surface tension of pure fluids: effect of molecular shape and polarity. *Physica A* **172**, 309–319 (1991). [https://doi.org/10.1016/0378-4371\(91\)90385-P](https://doi.org/10.1016/0378-4371(91)90385-P)
45. G.A. Fernández, J. Vrabec, H. Hasse, Self-diffusion and binary Maxwell-Stefan diffusion coefficients of quadrupolar real fluids from molecular simulation. *Int. J. Thermophys.* **26**, 1389–1407 (2005). <https://doi.org/10.1007/s10765-005-8093-6>
46. S. Homes, M. Heinen, J. Vrabec, Influence of molecular anisotropy and quadrupolar moment on evaporation. *Phys. Fluids* **35**, 052111 (2023). <https://doi.org/10.1063/5.0147306>
47. G.A. Fernandez, J. Vrabec, H. Hasse, Self diffusion and binary Maxwell-Stefan diffusion in simple fluids with the Green-Kubo method. *Int. J. Thermophys.* **25**, 175–186 (2004). <https://doi.org/10.1023/b:ijot.0000022333.07168.c4>
48. G.A. Fernández, J. Vrabec, H. Hasse, Shear viscosity and thermal conductivity of quadrupolar real fluids from molecular simulation. *Mol. Simul.* **31**, 787–793 (2005). <https://doi.org/10.1080/08927020500252599>
49. C. Mendiña, C. McBride, C. Vega, The second virial coefficient of quadrupolar two center Lennard-Jones models. *Phys. Chem. Chem. Phys.* **3**, 1289–1296 (2001). <https://doi.org/10.1039/B009509P>
50. C. Vega, C. McBride, C. Mendiña, The second virial coefficient of the dipolar two center Lennard-Jones model. *Phys. Chem. Chem. Phys.* **4**, 3000–3007 (2002). <https://doi.org/10.1039/B200781A>
51. K.E. Gubbins, Perturbation theories of the thermodynamics of polar and associating liquids: a historical perspective. *Fluid Phase Equilib.* **416**, 3–17 (2016). <https://doi.org/10.1016/j.fluid.2015.12.043>
52. C.H. Twu, K.E. Gubbins, Thermodynamics of polyatomic fluid mixtures-II: polar, quadrupolar and octopolar molecules. *Chem. Eng. Sci.* **33**, 879–887 (1978). [https://doi.org/10.1016/0009-2509\(78\)85177-X](https://doi.org/10.1016/0009-2509(78)85177-X)
53. J. Gross, An equation-of-state contribution for polar components: quadrupolar molecules. *AIChE J.* **51**, 2556–2568 (2005). <https://doi.org/10.1002/aic.10502>

54. B. Saager, J. Fischer, Construction and application of physically based equations of state: Part II. The dipolar and quadrupolar contributions to the Helmholtz energy. *Fluid Phase Equilib.* **72**, 67–88 (1992). [https://doi.org/10.1016/0378-3812\(92\)85019-5](https://doi.org/10.1016/0378-3812(92)85019-5)
55. K. Langenbach, Co-oriented fluid functional equation for electrostatic interactions (COFFEE). *Chem. Eng. Sci.* **174**, 40–55 (2017). <https://doi.org/10.1016/j.ces.2017.08.025>
56. E. Elts, T. Windmann, D. Staak, J. Vrabec, Fluid phase behavior from molecular simulation: Hydrazine, monomethylhydrazine, dimethylhydrazine and binary mixtures containing these compounds. *Fluid Phase Equilib.* **322–323**, 79–91 (2012). <https://doi.org/10.1016/j.fluid.2012.03.008>
57. F. Schiperski, A. Liebscher, M. Gottschalk, G. Franz, Re-examination of the heterotype solid solution between calcite and strontianite and Ca-Sr fluid-carbonate distribution: An experimental study of the  $\text{CaCO}_3\text{-SrCO}_3\text{-H}_2\text{O}$  system at 0.5–5 kbar and 600 °C. *Am. Miner.* **106**, 1016–1025 (2021). <https://doi.org/10.2138/am-2021-7783>
58. A. Liebscher, G. Dorsam, G. Franz, B. Wunder, M. Gottschalk, Ca-Sr fractionation between zoisite, lawsonite, and aqueous fluids: an experimental study at 2.0 and 4.0 GPa/400 to 800 °C. *Am. Miner.* **98**, 955–965 (2013). <https://doi.org/10.2138/am.2013.4279>
59. A. Szeri, Hydrodynamic and Elastohydrodynamic Lubrication in ‘Modern Tribology Handbook: Volume One: Principles of Tribology’, 1st edn. (CRC Press, Boca Raton, US, 2000)
60. P. Wingertzahn, S. Schmitt, S. Thielen, M. Oehler, B. Magyar, O. Koch, H. Hasse, S. Stephan, Measurement, modelling, and application of lubricant properties at extreme pressures. *Tribol. Schmierungstech.* **70**, 5–12 (2023). <https://doi.org/10.24053/tus-2023-0017>
61. S. Stephan, S. Schmitt, H. Hasse, H.M. Urbassek, Molecular dynamics simulation of the Stribeck curve: Boundary lubrication, mixed lubrication, and hydrodynamic lubrication on the atomistic level. *Friction* **11**, 2342–2366 (2023). <https://doi.org/10.1007/s40544-023-0745-y>
62. E.H. Brown, On the thermodynamic properties of fluids. *Bull. Inst. Int. Froid* **1960–1**, 169–178 (1960)
63. U.K. Deiters, K.M. De Reuck, Guidelines for publication of equations of state—I. Pure fluids. *Chem. Eng. J.* **69**, 69–81 (1998). [https://doi.org/10.1016/S1385-8947\(97\)00070-3](https://doi.org/10.1016/S1385-8947(97)00070-3)
64. M. Thol, G. Rutkai, R. Span, J. Vrabec, R. Lustig, Equation of state for the Lennard-Jones truncated and shifted model fluid. *Int. J. Thermophys.* **36**, 25 (2015). <https://doi.org/10.1007/s10765-014-1764-4>
65. R. Span, W. Wagner, On the extrapolation behavior of empirical equations of state. *Int. J. Thermophys.* **18**, 1415–1443 (1997). <https://doi.org/10.1007/BF02575343>
66. M. Thol, G. Rutkai, A. Koester, M. Kortmann, R. Span, J. Vrabec, Fundamental equation of state for ethylene oxide based on a hybrid dataset. *Chem. Eng. Sci.* **121**, 87–99 (2015). <https://doi.org/10.1016/j.ces.2014.07.051>
67. S. Pohl, R. Fingerhut, M. Thol, J. Vrabec, R. Span, Equation of state for the Mie ( $\lambda_r,6$ ) fluid with a repulsive exponent from 11 to 13. *J. Chem. Phys.* **158**, 084506 (2023). <https://doi.org/10.1063/5.0133412>
68. G. Chaparro, E.A. Müller, Development of thermodynamically consistent machine-learning equations of state: application to the Mie fluid. *J. Chem. Phys.* (2023). <https://doi.org/10.1063/5.0146634>
69. W. Wagner, A. Pruß, The IAPWS formulation 1995 for the thermodynamic properties of ordinary water substance for general and scientific use. *J. Phys. Chem. Ref. Data* **31**, 387–535 (2002). <https://doi.org/10.1063/1.1461829>
70. R. Span, W. Wagner, Equations of state for technical applications. I. Simultaneously optimized functional forms for nonpolar and polar fluids. *Int. J. Thermophys.* **24**, 1–39 (2003). <https://doi.org/10.1023/A:1022390430888>
71. J. Staubach, S. Stephan, Prediction of thermodynamic properties of fluids at extreme conditions: Assessment of the consistency of molecular-based models, in *Proceedings of the 3rd Conference on Physical Modeling for Virtual Manufacturing Systems and Processes*. ed. by J.C. Aurich, C. Garth, B.S. Linke (Springer, Cham, 2023), pp.170–188
72. S. Stephan, U.K. Deiters, Characteristic curves of the Lennard-Jones fluid. *Int. J. Thermophys.* **41**, 147 (2020). <https://doi.org/10.1007/s10765-020-02721-9>
73. S. Stephan, M. Urschel, Characteristic curves of the Mie fluid **383**, 122088 <https://doi.org/10.1016/j.molliq.2023.122088>
74. O.L. Boshkova, U.K. Deiters, Soft repulsion and the behavior of equations of state at high pressures. *Int. J. Thermophys.* **31**, 227–252 (2010). <https://doi.org/10.1007/s10765-010-0727-7>

75. A. Neumaier, U.K. Deiters, The characteristic curves of water. *Int. J. Thermophys.* **37**, 96 (2016). <https://doi.org/10.1007/s10765-016-2098-1>
76. U.K. Deiters, A. Neumaier, Computer simulation of the characteristic curves of pure fluids. *J. Chem. Eng. Data* **61**, 2720–2728 (2016). <https://doi.org/10.1021/acs.jced.6b00133>
77. M. Urschel, S. Stephan, Determining Brown's characteristic curves using molecular simulation. *J. Chem. Theory Comput.* **5**, 1537–1552 (2023). <https://doi.org/10.1021/acs.jctc.2c01102>
78. J. Vrabec, G.K. Kedja, H. Hasse, Prediction of Joule-Thomson inversion curves for pure fluids and one mixture by molecular simulation. *Cryogenics* **45**, 253–258 (2005). <https://doi.org/10.1016/j.cryogenics.2004.10.006>
79. J. Vrabec, A. Kumar, H. Hasse, Joule-Thomson inversion curves of mixtures by molecular simulation in comparison to advanced equations of state: Natural gas as an example. *Fluid Phase Equilib.* **258**, 34–40 (2007). <https://doi.org/10.1016/j.fluid.2007.05.024>
80. C.G. Aimoli, E.J. Maginn, C.R.A. Abreu, Thermodynamic properties of supercritical mixtures of carbon dioxide and methane: a molecular simulation study. *J. Chem. Eng. Data* **59**, 3041–3054 (2014). <https://doi.org/10.1021/je500120v>
81. S. Figueroa-Gerstenmaier, M. Lísal, I. Nezbeda, W.R. Smith, V.M. Trejos, Prediction of isenthalps, Joule-Thomson coefficients and Joule-Thomson inversion curves of refrigerants by molecular simulation. *Fluid Phase Equilib.* **375**, 143–151 (2014). <https://doi.org/10.1016/j.fluid.2014.05.011>
82. C.M. Colina, E.A. Müller, Molecular simulation of Joule-Thomson inversion curves. *Int. J. Thermophys.* **20**, 229–235 (1999). <https://doi.org/10.1023/A:1021402902877>
83. C. Colina, E.A. Müller, Joule-Thomson inversion curves by molecular simulation. *Mol. Sim.* **19**, 237–246 (1997). <https://doi.org/10.1080/08927029708024153>
84. C.M. Colina, M. Lísal, F.R. Siperstein, K.E. Gubbins, Accurate CO<sub>2</sub> Joule-Thomson inversion curve by molecular simulations. *Fluid Phase Equilib.* **202**, 253–262 (2002). [https://doi.org/10.1016/S0378-3812\(02\)00126-7](https://doi.org/10.1016/S0378-3812(02)00126-7)
85. A. Chacin, J.M. Vazquez, E.A. Mueller, Molecular simulation of the Joule-Thomson inversion curve of carbon dioxide. *Fluid Phase Equilib.* **165**, 147–155 (1999). [https://doi.org/10.1016/S0378-3812\(99\)00264-2](https://doi.org/10.1016/S0378-3812(99)00264-2)
86. J. Rößler, I. Antolovic, S. Stephan, J. Vrabec, Assessment of thermodynamic models via Joule-Thomson inversion. *Fluid Phase Equilib.* **556**, 113401 (2022). <https://doi.org/10.1016/j.fluid.2022.113401>
87. M.H. Lagache, P. Ungerer, A. Boutin, Prediction of thermodynamic derivative properties of natural condensate gases at high pressure by Monte Carlo simulation. *Fluid Phase Equilib.* **220**, 211–223 (2004). <https://doi.org/10.1016/j.fluid.2004.03.015>
88. M. Lísal, K. Aim, M. Mecke, J. Fischer, Revised equation of state for two-center Lennard-Jones fluids. *Int. J. Thermophys.* **25**, 159–173 (2004). <https://doi.org/10.1023/B:IJOT.0000022332.12319.06>
89. R. Fingerhut, G. Guevara-Carrion, I. Nitzke, D. Saric, J. Marx, K. Langenbach, S. Prokopev, D. Celný, M. Bernreuther, S. Stephan, M. Kohns, H. Hasse, J. Vrabec, ms2: A molecular simulation tool for thermodynamic properties, release 4.0. *Comput. Phys. Commun.* **262**, 107860 (2021). <https://doi.org/10.1016/j.cpc.2021.107860>
90. G. Rutkai, A. Köster, G. Guevara-Carrion, T. Janzen, M. Schappals, C.W. Glass, M. Bernreuther, A. Wafai, S. Stephan, M. Kohns, S. Reiser, S. Deublein, M. Horsch, H. Hasse, J. Vrabec, ms2: A molecular simulation tool for thermodynamic properties, release 3.0. *Comput. Phys. Commun.* **221**, 343–351 (2017). <https://doi.org/10.1016/j.cpc.2017.07.025>
91. L. Xu, Y.-Y. Duan, H.-T. Liu, Z. Yang, Empirical correlations for second virial coefficients of non-polar and polar fluids covering a wide temperature range. *Fluid Phase Equilib.* **539**, 113032 (2021). <https://doi.org/10.1016/j.fluid.2021.113032>
92. R. Lustig, Direct molecular NVT simulation of the isobaric heat capacity, speed of sound and Joule-Thomson coefficient. *Mol. Simul.* **37**, 457–465 (2011). <https://doi.org/10.1080/08927022.2011.552244>
93. R. Lustig, Statistical analogues for fundamental equation of state derivatives. *Mol. Phys.* **110**, 3041–3052 (2012). <https://doi.org/10.1080/00268976.2012.695032>
94. T. Boublík, I. Nezbeda, P-v-t behaviour of hard body fluids. theory and experiment. *Collect. Czech. Chem. Commun.* **51**, 2301–2432 (1986). <https://doi.org/10.1135/cccc19862301>
95. M. Mecke, A. Müller, J. Winkelmann, J. Fischer, An equation of state for two-center Lennard-Jones fluids. *Int. J. Thermophys.* **18**, 683–698 (1997). <https://doi.org/10.1007/bf02575128>

96. S. Stephan, J. Staubach, H. Hasse, Review and comparison of equations of state for the Lennard-Jones fluid. *Fluid Phase Equilib.* **523**, 112772 (2020). <https://doi.org/10.1016/j.fluid.2020.112772>
97. E.M. Apfelbaum, V.S. Vorob'ev, G.A. Martynov, Triangle of liquid-gas states. *J. Phys. Chem. B* **110**, 8474–8480 (2006). <https://doi.org/10.1021/jp057327c>
98. E.M. Apfelbaum, V.S. Vorob'ev, G.A. Martynov, Regarding the theory of the Zeno line. *J. Phys. Chem. A* **112**, 6042–6044 (2008). <https://doi.org/10.1021/jp802999z>
99. K.S. Pitzer, Corresponding states for perfect liquids. *J. Chem. Phys.* **7**, 583–590 (1939). <https://doi.org/10.1063/1.1750496>
100. E.A. Guggenheim, The principle of corresponding states. *J. Chem. Phys.* **13**, 253–261 (1945). <https://doi.org/10.1063/1.1724033>

**Publisher's Note** Springer Nature remains neutral with regard to jurisdictional claims in published maps and institutional affiliations.